Development and maintenance of fluid overpressures in crustal fault zones by elastic compaction and implications for earthquake swarms

H. Leclère, F. Cappa, D. Faulkner, O. Fabbri, P. Armitage, O. Blake

AGU PUBLICATIONS

JGR

Journal of Geophysical Research: Solid Earth

RESEARCH ARTICLE
10.1002/2014JB011759

Key Points:
- Fault zone is characterized by heterogeneous hydraulic and elastic properties
- Fluid overpressures can be developed and maintained in heterogeneous fault zones
- Elastic compaction is a viable mechanism to trigger seismic activity

Correspondence to:
H. Leclère,
henri.leclere@liverpool.ac.uk

Citation:
Leclère, H., F. Cappa, D. Faulkner, O. Fabbri, P. Armitage, and O. Blake (2015), Development and maintenance of fluid overpressures in crustal fault zones by elastic compaction and implications for earthquake swarms, *J. Geophys. Res. Solid Earth*, *120*, 4450–4473, doi:10.1002/2014JB011759.

Received 10 NOV 2014
Accepted 5 MAY 2015
Accepted article online 7 MAY 2015
Published online 10 JUN 2015

Development and maintenance of fluid overpressures in crustal fault zones by elastic compaction and implications for earthquake swarms

Henri Leclère[1,2], Frédéric Cappa[3], Daniel Faulkner[2], Olivier Fabbri[1], Peter Armitage[4], and Oshaine Blake[5]

[1]Chrono-Environnement (UMR 6249), University of Bourgogne-Franche-Comté, Besançon, France, [2]Rock Deformation Laboratory, Department of Earth, Ocean and Ecological Sciences, University of Liverpool, Liverpool, UK, [3]Geoazur (UMR7329), University of Nice Sophia-Antipolis, CNRS, IRD, Côte d'Azur Observatory, Nice, France, [4]BP Exploration Operating Company, Sunbury-on-Thames, UK, [5]Petroleum Geoscience Program, Department of Chemical Engineering, University of the West Indies, St. Augustine, Trinidad and Tobago

Abstract The ability of crustal faults to compact and to pressurize pore fluids is examined by combining geological observations, petrophysical measurements (permeability, *P* and *S* wave velocities, and porosity), and fully coupled hydromechanical modeling. A strike-slip fault located in the Argentera-Mercantour crystalline massif (southwestern French-Italian Alps) was analyzed in the field. This mature fault belongs to a large active fault system characterized by a recurrent seismic swarm activity ($M_w < 4$) between 2 and 12 km depth. The studied exposure corresponds to a 50 m thick anastomosing fault composed of three types of rock: host-rock gneiss, damage-zone phyllonite, and core zone gouge. Laboratory measurements made at effective pressures ranging from 10 to 190 MPa show that the studied fault differs from the classical model and has a high-porosity, high-permeability, and low-rigidity core zone surrounded by a low-porosity, low-permeability, and high-rigidity damage zone with respect to the host rock. The hydraulic and elastic properties are controlled by different microstructures such as foliation, microcracks, and pores developed during the exhumation history of the massif and the reactivation of inherited low-friction mylonitic foliation. Hydromechanical modeling is then used to investigate the spatio-temporal evolution of the fluid overpressures across the fault zone elements in response to elastic compaction. Models demonstrate that fluid pressure can be developed and maintained temporally in the studied fault zone. This study concludes on the key role played by the hydromechanical properties of faults during compaction and provides an explanation for seismic swarm triggering and maintenance.

1. Introduction

In the upper seismogenic crust, fluid pressurization is a viable mechanism for fault weakening and for earthquake triggering. However, the generation, maintenance, and diffusion of fluid overpressures in faults remain unclear. The presence of fluids in crustal faults is evidenced by various types of geological, geophysical, and geochemical data, and it is widely recognized that these fluids affect fault mechanics and play an important role in the seismic cycle [*Sibson*, 1990]. In particular, the presence of overpressured fluids in faults is often invoked to explain the apparent weakness of misoriented faults with respect to the stress field by reducing the effective normal stress [*Rice*, 1992; *Collettini and Sibson*, 2001; *Faulkner et al.*, 2006; *Mittempergher et al.*, 2009; *Leclère et al.*, 2012a]. Thus, the mechanisms of development, maintenance, and diffusion of such high fluid pressures in faults are key issues for fault mechanics, and several models have been proposed to explain fluid pressure buildup in faults.

Nur and Booker [1972] introduced the "dilatancy-fluid-diffusion" model in which pore pressures develop by the closure of cracks saturated with fluid following an earthquake. The relaxation of cracks reduces the total volume of the rock and induces fluid pressure buildup. This model was used to explain the deformation, fluid flow, and gravity measurements recorded during the 1969 Matsushiro earthquake swarm [*Nur*, 1974].

Sibson [1990] proposed the "fault-valve" model. In this model, fluids are supplied from depth (e.g., mineral dehydration during prograde metamorphism or mantle degassing) and are trapped beneath a hydraulic barrier preventing fluid to escape vertically and allowing fluid pressure to build up to a critical value

corresponding to the resistance of the barrier. When fluid overpressures exceed the strength of the barrier, the fluid can escape upward and can possibly overpressurize faults located above the barrier. This model was used to explain seismic migration, aftershock sequences, and tectonic inversion in many instances [*Miller et al*., 2004; *Sibson*, 2009; *Terakawa et al*., 2010].

Rice [1992] proposed a model where fluid overpressures are developed and maintained by continuous fluid flow coming from below. In this model, fluid pressure is maintained in the core of the fault zone if the loss of the fluid pressure is low enough to be compensated by the injection of fluid from depth. This theoretical model was tested by *Faulkner and Rutter* [2001] who used field and laboratory data on the Carboneras fault and who concluded that fluid overpressures can be maintained with only a small fluid flux from depth.

Lastly, *Blanpied et al*. [1992], *Sleep and Blanpied* [1992], and *Byerlee* [1993] explain the generation of fluid overpressures by the reduction of porosity during compaction of faults. In this model, the fault is seen as a thick zone composed of a fluid-saturated core gouge sensitive to compaction and surrounded by an impervious damage zone. During stress increase, compaction and healing of the fault core zone lead to a reduction of the porosity and to an increase of the fluid pressure. This model was used by *Gratier et al*. [2003] to explain the development of fluid overpressures during the interseismic period along the San Andreas fault system.

In this study, we provide a quantitative analysis on how elastic compaction, induced by Coulomb stress transfer following an earthquake, can produce fluid overpressure in a mature crustal fault with lateral variations of hydraulic and elastic properties in the internal structure, and how long the fluid overpressure can be maintained in the fault zone. To address this question, our study combines structural geology, laboratory measurements, and hydromechanical modeling. The geological analysis is carried out on a crustal strike-slip fault exposure located in the Argentera-Mercantour massif (southwestern French-Italian Alps) that belongs to a large active fault system characterized by recurrent seismic swarm activities ($M_w < 4$) associated with fluid overpressures [*Jenatton et al*., 2007; *Daniel et al*., 2011; *Leclère et al*., 2012a, 2013]. The 2003–2004 Ubaye seismic swarm (16,000 events) occurred in the crystalline basement at a 7 km mean hypocentral depth and is located 40 km northward along strike of the analyzed fault. Therefore, the studied outcrop can be considered as representative of an exhumed portion of the seismogenic zone of the 2003–2004 Ubaye swarm [*Leclère et al*., 2012a]. *Leclère et al*. [2013] furthermore suggested that fluid overpressures were developed by creep compaction during the swarm activity and were maintained for about 1 year in two distinct patches of the fault surface. The second objective of our study is thus to validate if the compaction of a fault is a viable mechanism allowing the development and maintenance of fluid overpressures triggering seismic swarm activity over these periods.

The paper is organized in five sections. Following the introduction (section 1), section 2 presents the geological setting of the study area and describes the studied fault. Section 3 presents the laboratory methods and the hydraulic and elastic properties of the constitutive materials of the studied fault. Section 4 discusses the microstructures controlling the hydraulic and elastic properties of the fault. Then section 5 presents the hydromechanical modeling and the influences of the elastic and hydraulic properties of the core zones, the damage zones, and the host rock on the development and maintenance of fluid pressures inside the fault zone. Lastly, we discuss in section 6 the structural and physical properties of the fault allowing the development and maintenance of fluid overpressures and their implications on the understanding of seismic swarm activity.

2. Geological Context and Internal Structure of the Studied Fault

The studied fault is situated in the Argentera-Mercantour (AM) massif, one of the external crystalline massifs of the southwestern French-Italian Alps [e.g., *Schmid et al*., 2004] (Figure 1a). The massif is mainly composed of Variscan migmatitic paragneisses and orthogneisses and intrusive granitoids (Figure 1). It is crosscut by several NW-SE ductile shear zones steeply dipping toward the NE or SW (Figure 1b). By "ductile" we mean flow of rocks accommodated by intracrystalline plasticity or diffusion. The main shear zone is the Valetta Shear Zone (VSZ) [*Faure-Muret*, 1955; *Bogdanoff*, 1986], also known as the Ferriere-Mollières Line [*Malaroda et al*., 1970] (Figure 1a). The VSZ connects to the Bersezio fault (BF) in the central part of the Argentera massif and is made up of mylonitic rocks that formed during Variscan and Alpine orogeneses (Figure 1) [*Musumeci and Colombo*, 2002; *Corsini et al*., 2004; *Sanchez et al*., 2011a]. The VSZ and BZ delineate a

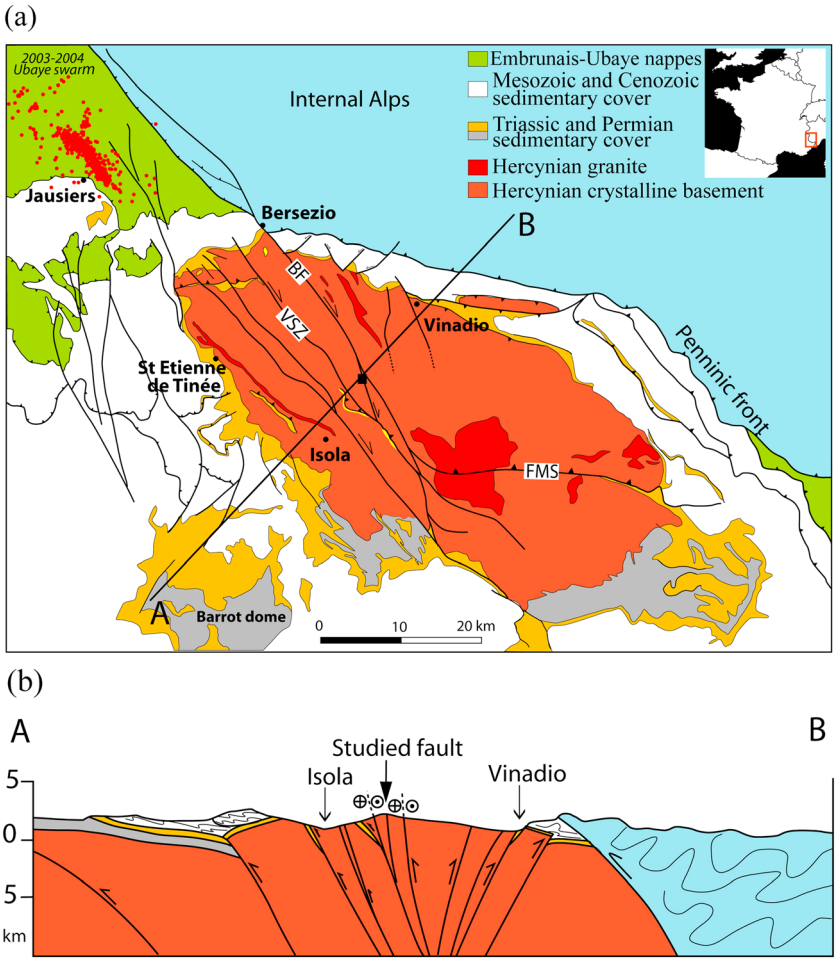

Figure 1. Geological setting of the studied area. (a) Simplified geological map (modified after *Kerckhove et al.* [1980]). BZ: Bersezio Fault; VSZ: Valetta Shear Zone; FMS: Fremamorta Shear Zone. Red dots correspond to the hypocenters of the 2003–2004 Ubaye seismic swarm. The black square indicates the location of the studied fault zone. (b) Cross-section of the Argentera-Mercantour massif.

several hundred meters thick shear zone composed of anastomosed faults. Northwestward, the AM crystalline rocks and associated shear zones disappear beneath an autochthonous sedimentary cover composed of marls (including notably 300 m thick Jurassic marls), sandstones, limestones, and evaporites. This sedimentary cover is in turn overlain by a pile of two nappes (so-called Embrunais-Ubaye nappes) consisting of nonmetamorphic calcareous turbidites. Only a part of the faults cutting the crystalline basement also cuts the post-Variscan sedimentary pile (sedimentary cover and sedimentary nappes). As will be taken into account in the model, the sedimentary pile, whose thickness is between 1 and 2 km, is significantly less faulted than the underlying basement and is considered to act as an impervious lid preventing or hindering the vertical fluid flows, either downward (rainfall or snow melt infiltration) or upward (e.g., thermal springs).

The Argentera-Mercantour massif experienced Variscan and Alpine deformation. The Variscan orogenesis is characterized by a polyphase deformation history with early eclogitic and granulitic metamorphisms followed by a migmatitic high-temperature metamorphism [*Monié and Maluski*, 1983; *Paquette et al.*, 1989; *Rubatto et al.*, 2001]. The emplacement of the Argentera granite during the Upper Stephanian/Lower Permian marks the end of the high-temperature metamorphism and associated melting [*Ferrara and Malaroda*, 1969]. Alpine tectonics in the AM are represented by crustal-scale imbrications and subsequent uplift of the crystalline basement [*Kerckhove*, 1969; *Bogdanoff*, 1986] and by the reactivation of Variscan shear zones such as the VSZ in the ductile to brittle regime of deformation [*Bogdanoff et al.*, 2000;

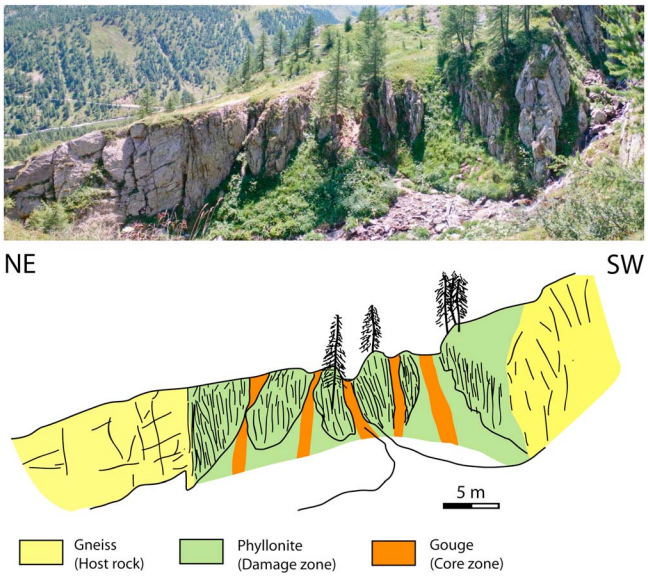

Figure 2. Photograph and corresponding sketch of the studied outcrop. The fault zone shows anastomosed core zones surrounded by damage zones with a pluri-decametric total width. The core zones are made of centimetric to metric phyllosilicate-rich gouge layers. The damage zones are composed of pluri-metric phyllonitic rocks derived from mylonite. The host rock is composed of gneiss.

Corsini et al., 2004; *Bigot-Cormier et al.*, 2006; *Baietto et al.*, 2009; *Sanchez et al.*, 2011a, 2011b]. Alpine ductile shearing occurred under the greenschist facies conditions and is dated by the ^{39}Ar-^{40}Ar method on synkinematic phengites within the mylonites of the Fremamorta Shear Zone (FMS) [*Corsini et al.*, 2004] and VSZ [*Sanchez et al.*, 2011a]. According to these authors, the ductile deformation occurred at circa 22.5 Ma and the T-P estimates are 350°C and 350–400 MPa, which imply a burial of ~14 km (assuming a mean geothermal gradient of 25°C/km) for the AM. In the field, the brittle regime of deformation is attested by breccias and gouges overprinting the mylonites.

The analyzed fault exposure (black square in Figure 1a) is located in the central part of the Argentera massif, between Isola and Vinadio villages. The studied fault belongs to a dextral strike-slip fault zone striking N150°E, dipping 80°NE, and linking the Bersezio fault to the Valetta shear zone. The analyzed outcrop consists of a 50 m thick corridor composed of multiple anastomosed strands of gouge surrounded by highly foliated phyllonitic rocks (Figures 2, 3a, and 3b). The offset of the fault is unknown due to the lack of geological markers. However, based on the total thickness of the core zone and the damage zone, the total horizontal offset could be of the scale of the hectometer [*Shipton et al.*, 2006].

The intact host rock is a gneiss composed of quartz, K-feldspar, plagioclase, biotite, and muscovite [*Bogdanoff*, 1986; *Sanchez et al.*, 2011a]. Biotite and muscovite are found along parallel millimeter thick ribbons and define the gneissic foliation S1 (Figure 3c). The foliation strikes N-S, dips steeply, and bears a horizontal mineral lineation.

The damage-zone compartments are composed of phyllonitic rocks derived from mylonite (Figure 3d). The phyllonite shows subhorizontal stepped slickenlines indicating a right-lateral sense of motion. The phyllonite consists of quartz, plagioclase, chlorite, and muscovite. The phyllonitic fabric is characterized by a S-C structure defined by the alignment of phyllosilicates. The S-C structure is steeply dipping with C planes striking N140°E, parallel to the fault strike.

The core zone strands are made up of centimetric to pluridecimetric gouge layers (Figures 2, 3a, and 3b). The gouge is composed of polymineralic grains of quartz and feldspar and of inherited or newly formed chlorite and muscovite. The gouge displays a steeply dipping foliation parallel to the fault. The foliation is characterized by millimeter to centimeter thick fine-grained phyllosilicate-rich layers displaying S-C structures and by millimeter to centimeter thick coarse-grained microbreccia layers composed of quartz and feldspar (Figure 3e). S-C structures indicate a dextral strike-slip sense of motion.

3. Permeability, Porosity, and Elastic Wave Velocity Measurements

3.1. Sample Preparation and Methods

Representative samples of gneiss, phyllonite, and gouge were taken from the host rock, through the damage zone to the core zone. Cores with a diameter of 20 mm and lengths between 26 and 51 mm were drilled in gneiss and phyllonite samples. Gouge was sampled using the method described by *Faulkner and Rutter* [1998]. The visible weathered surface was cut away from the exposure until a significant volume of rock free from cracks and major heterogeneities was exposed. Sharpened copper tubes, 20 mm in internal

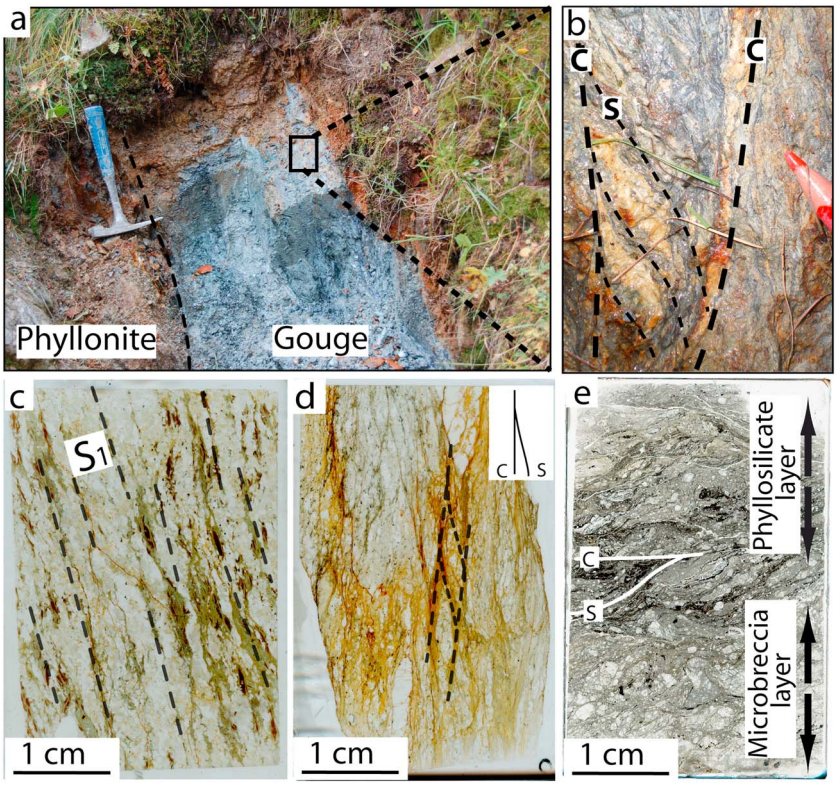

Figure 3. Macroscale to microscale photographs of gneiss, phyllonite, and gouge. (a) Contact between phyllonite and gouge. (b) Foliated gouge showing foliation (S) and shear surfaces (C), the arrangement of which indicating a right-lateral sense of shear. (c) Foliation (S1) in intact gneiss (scan of thin section). (d) Phyllonite showing an S-C-like structure (scan of thin section). (e) Gouge showing fine-grained phyllosilicate-rich layers, coarse-grained microbreccia layers, and S-C-like structures (scan of thin section).

diameter, were hammered into this soft material. In the laboratory, the walls of the copper tubes (originally 1 mm in thickness) were thinned to 0.5 mm. This thickness maintains the integrity of the gouge but is thin enough not to support the confining pressure applied to the gouge samples during the experiments. Gouge cores were longer than gneiss or phyllonite cores. A first category of gouge cores, identified with the subscript *a* ($k_{H\text{-}a}$, $k_{h\text{-}a}$, and $k_{v\text{-}a}$, see below), had maximum lengths of 50 mm ± 5 mm. A second category, identified with the subscript *b* (named $k_{H\text{-}b}$, $k_{h\text{-}b}$, and $k_{v\text{-}b}$, see below), had lengths of 80 mm ± 5 mm. The 80 mm long cores allow testing the influences of the millimeter to centimeter thick fine-grained phyllosilicate-rich layers and coarse-grained microbreccia layers on the hydraulic and elastic properties.

Cores were drilled in three perpendicular directions with respect to the orientations of the foliation planes (F) or shear planes (C) and of the lineation (L) or slickenlines. The direction of the lineation or slickenlines is hereafter called transport direction (TD). A set of cores (k_h) were drilled perpendicular to C or F. This direction is subhorizontal and perpendicular to the fault. A set of cores (k_H) were drilled parallel to C or F and parallel to the L or TD. This direction is nearly horizontal and parallel to the fault. Finally, a set of cores (k_v) were drilled parallel to C or F and perpendicular to L or TD. This direction is close to vertical.

The permeability and elastic wave velocities of gneiss, phyllonite, and gouge cores were measured with a high-pressure hydrostatic fluid-flow apparatus equipped with an ultrasonic system (Figure 4). Details of the hydrostatic apparatus can be found in *Armitage et al.* [2011]. The apparatus uses silicon oil as a confining medium and argon gas as the permeant. Before experiments, the ends of the cores of rocks were squared to a tolerance ≤0.2 mm. Samples were oven dried at 80°C for ≥24 h to remove free water. The cores were then placed in the sample assembly as shown in Figure 4a. A jacket of PVC with a wall thickness of 3.5 mm prevents silicon oil from penetrating into the samples. Two 3 mm thick porous stainless steel spacers with a nominal permeability of 1.3×10^{-13} m^2 were placed at the two ends of the sample to ensure uniform

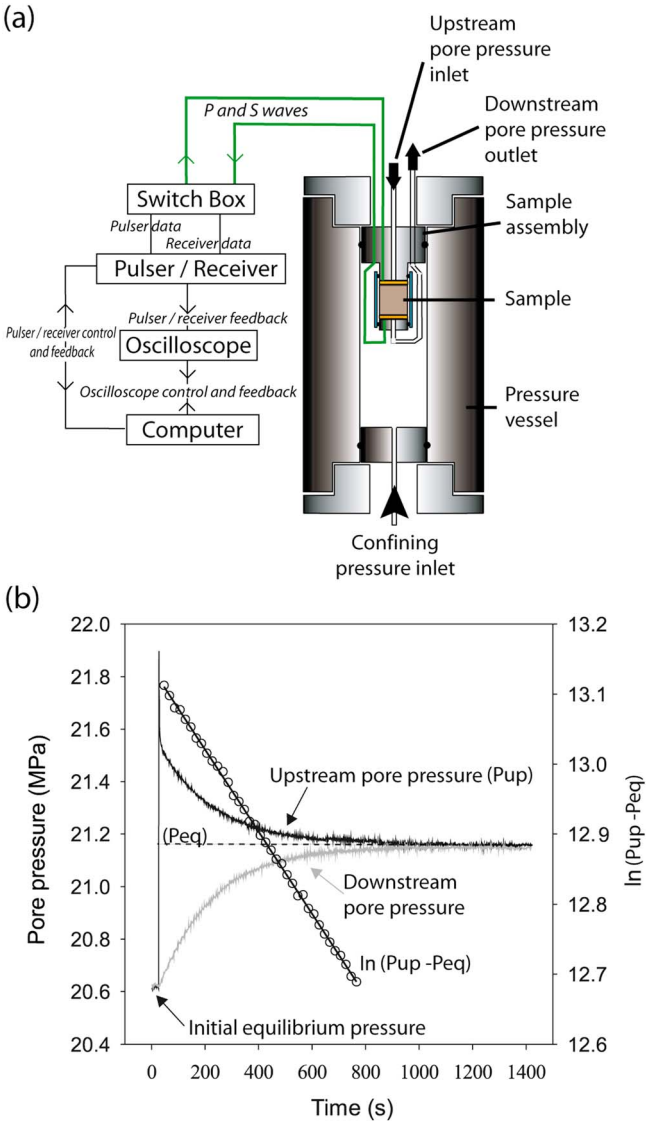

Figure 4. Techniques and methods of the laboratory measurements (modified from *Armitage et al.* [2011]). (a) Description of the high-pressure hydrostatic fluid flow apparatus equipped with an ultrasonic system. (b) Method of permeability determination from the transient pulse decay (TPD) technique.

pressure distribution over the faces of the sample. After loading the sample assembly into the experimental apparatus, the confining pressure and pore pressure were increased incrementally to the conditions of the first measurement, ensuring that the effective pressure at which the first measurements were to be made was never exceeded. The measurements were performed at room temperature (~22°C) with a constant pore fluid pressure of 20 MPa and with confining pressures ranging from 30 MPa to 210 MPa, with steps of 30 MPa.

The permeability was measured by the transient pulse decay (TPD) technique [*Brace et al.*, 1968]. The method consists of introducing a pressure step of approximately 1 MPa across the sample. The pressure at the upstream end of the core decays as the pore fluid flows through the sample. The downstream pore pressure consequently increases (Figure 4b). The evolution of the pressure of the upstream reservoir through time can be solved by the following equation:

$$P_{up} - P_{eq} = \Delta P\left[\left(\frac{V_2}{V_1 + V_2}\right)\right]e^{-\lambda t} \quad (1)$$

where P_{up} is the pressure of the upstream reservoir (MPa), P_{eq} is the equilibrium pressure (MPa), ΔP is the step variation of P_{up} at the start of the measurement (MPa), V_1 and V_2 are the volumes of the upstream and downstream reservoir (m^3), and λ is the slope of straight line $\ln(P_{up}-P_{eq})$ as a function of time (Figure 4).

Based on the value of λ, the permeability values can be obtained from the following equation:

$$\lambda = \frac{kA}{\beta\eta L}\left(\frac{1}{V_1} + \frac{1}{V_2}\right) \quad (2)$$

where k is the intrinsic permeability (m^2), A is the cross-sectional area of the core (m^2), β is the fluid compressibility (Pa^{-1}), η is the fluid viscosity (Pa. s), and L is the length of the core (m).

The TPD method allows the mean permeability for a selected period of time to be computed by determining the slope λ from the linear regression of the recording. This permeability value is representative for a signal without noise. In order to analyze the errors on the permeability measurements, a bootstrapping method was developed. The method allows estimation of the variation of the permeability by bootstrapping the signal and computing the permeability in several time windows. The computation starts at the initial time t_0 and computes the permeability values for each time interval between t_0 and $t_0 + n.x$, where n is the duration interval and x is the number of computation. When $t_0 + n.x$ equals the total duration of the recording, t_0 is

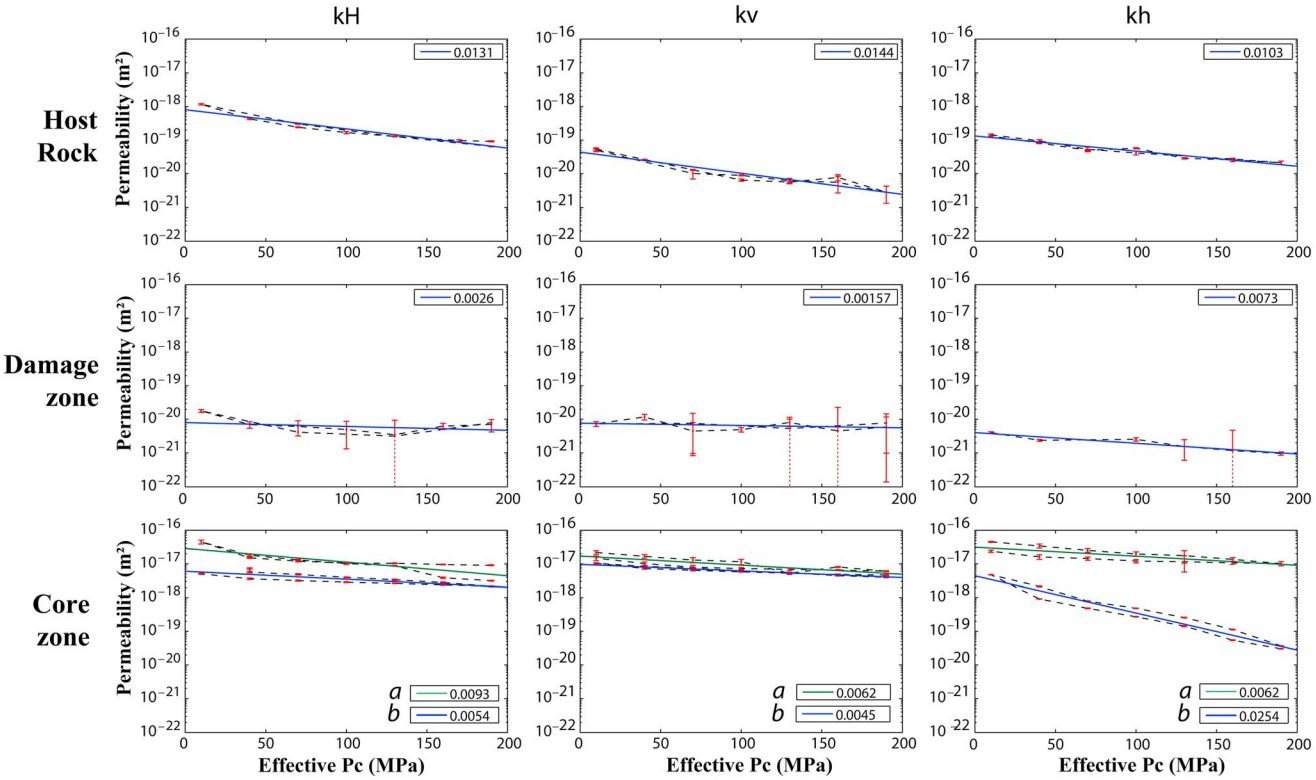

Figure 5. Permeability measurement results for gneiss, phyllonite, and gouge samples performed in three directions. Vertical red bars correspond to the range permeability measurements where the extremities refer to the standard deviation and where red dots to the median value. Blue and green lines represent the linear regression of the permeability versus confining pressure. Numbers at the right side top or bottom corners refer to the sensitivity of permeability to the confining pressure γ and correspond to the slope of the blue or the green lines. The term k_v refers to the vertical direction, k_h refers to the horizontal direction perpendicular to the fault, and k_H refers to the horizontal direction parallel to the fault.

increased to n and the bootstrapping starts again. Bootstrapping ends when t_0 is equal to the duration of the signal. Here the duration interval n is between 20 and 120 s. The duration interval is fixed following the duration of the recording which is function of the permeability of the sample. Indeed, the lower the permeability of the sample, the more time is needed to compute permeability and the greater time interval n is required to discard effects of local slope perturbation.

Results of permeability measurements are given as the median and the standard deviation values of the set of permeability values obtained from the bootstrapping method (Figure 5). Here the regression coefficients r range from 0.99 for acceptable signals to 0.40 for noisy signals. In Figure 5, medians are represented by red dots while standard deviations by red vertical error bars. Some errors bars are represented by dashed lines, which correspond to permeability results for which the standard deviation is larger than the median value. In such cases, the minimum permeability value expected by the statistical analysis is negative. Consequently, for these permeability measurements, the analysis only provides an upper bound on the permeability.

At the same time as the permeability measurements, *P* and *S* wave velocities of gneiss, phyllonite, and gouge cores were measured in order to estimate the elastic moduli. To record the elastic wave travel time, two different types of piezoelectric ceramics, one *P* wave and one *S* wave with a fundamental frequency of 1.5 MHz, are housed in each porous stainless steel spacer of the sample assembly (Figure 4a). For a description of the apparatus and techniques used, see *Blake et al.* [2013]. A through-transmission method was employed to measure the *P* and *S* wave velocity of the sample in the axial direction. The pulsing *P* and *S* wave piezoelectric ceramics were aligned with receiving *P* and *S* wave piezoelectric ceramics, respectively. A negative spike pulser/receiver (JSR DPR300 Pulser/Receiver) was used for excitation of the piezoelectric ceramics and detection of the pulse. The choice of piezoelectric ceramics to transmit or receive is manually controlled by a switch box. A 300 MHz bandwidth digital oscilloscope with 20 ppm time-based accuracy (Tektronix TDS 3032B) was used for recording the received pulse which is

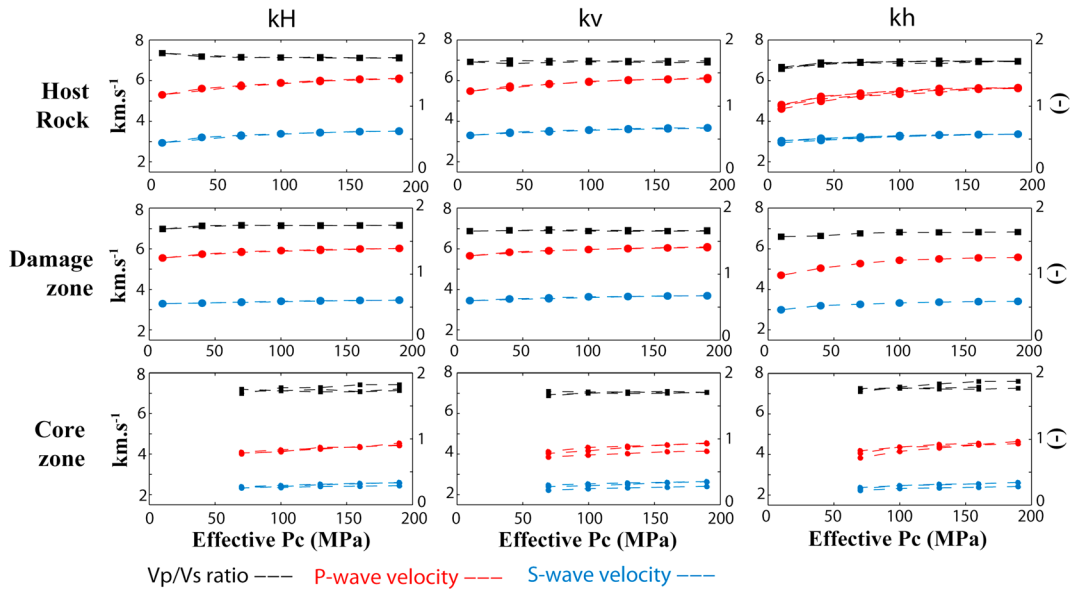

Figure 6. V_P and V_S measurements and V_P/V_S ratios for gneiss, phyllonite, and gouge samples performed in three directions. The term k_v refers to the vertical direction, k_h refers to the horizontal direction perpendicular to the fault, and k_H refers to the horizontal direction parallel to the fault.

synchronized with the pulser/receiver. The transmitter/receiver and oscilloscope are coupled to a computer for data storage and processing of the recorded waveforms for analysis.

The porosity of gneiss and phyllonite samples was measured using Archimedes method to quantify connected porosity of the drilled plugs. The samples were dried at 60°C until they reached a stable mass (m_d), then placed under vacuum for 12 h before being progressively saturated with degassed and distilled water. The connected porosity (Nt) is given by $Nt = [(m_2 - m_d)/(m_2 - m_1)] \times 100$, where m_1 is the mass of the sample totally saturated by water weighed under water (hydrostatic weighing) and m_2 is the mass of the sample totally saturated by water. The porosity of the gouge cores was measured after experiments with a He-pycnometer. The pycnometer measurements were repeated 3 times for each sample in order to obtain representative values.

3.2. Results

Measured permeability and elastic wave velocity data are presented graphically as a function of effective stress in Figures 5 and 6 and are summarized in Table 1. The permeability values range from 10^{-17} to

Table 1. Permeability, V_P, V_S and Porosity Laboratory Measurements for Gneiss, Phyllonite and Gouge

		Permeability Between 10 and 190 MPa (×10–21)			V_P Between70 and 190 MPa (m s^{-1})		V_S Between 70 and 190 MPa (m s^{-1})		Porosity Nt (%)		
Samples	Orientation	Min	Max	γ	Min	Max	Min	Max	Min	Mean	Max
Gneiss (host rock)	kH	64.48	1,160	0.0131	5,726	6,105	3,291	3,532	1.9	2.2	2.7
	kh	21.20	143	0.0144	5,246	5,659	3,172	3,373			
	kv	2.81	53.91	0.0103	5,817	6,119	3,470	3,659			
Phyllonite (damage zone)	kH	3.14	17.8	0.0026	5,823	6,017	3,352	3,468	1.4	1.6	2.2
	kh	0.96	4.01	0.0073	5,277	5,574	3,254	3,394			
	kv	4.49	11.8	0.0015	5,881	6,075	3,526	3,671			
Gouge (core zone)	kH-a	2,153	7,298	0.0093	4,035	4,528	2,308	2,583	14.7	16.9	18.6
	kH-b	3,164	44,922	0.0054	3,993	4,399	2,329	2,423			
	kh-a	10,161	45,250	0.0062	4,055	4,636	2,312	2,617			
	kh-b	30.27	4,741	0.0254	3,830	4,524	2,229	2,415			
	kv-a	5,233	21,836	0.0062	3,976	4,478	2,375	2,618			
	kv-b	3,974	10,402	0.0045	3,880	4,159	2,252	2,435			

10^{-22} m^2 with values between 2.81×10^{-21} and 1.16×10^{-18} m^2 for gneiss, 9.6×10^{-22} and 1.78×10^{-20} m^2 for phyllonite, and 3.03×10^{-20} and 4.52×10^{-17} for gouge. The permeability values for gneiss samples are similar to the laboratory measurements performed by *Morrow et al*. [1994] on granodiorite gneisses from the Kola borehole in Russia and from the KTB borehole in Germany. These authors showed a reduction of the matrix permeability from 10^{-17} to 10^{-22} m^2 when increasing the effective pressure from 5 to 300 MPa. The permeability values for phyllonite samples are in the range obtained in previous studies (10^{-18} to 10^{-21} m^2) for mylonitic or cemented rocks [*Wibberley and Shimamoto*, 2003; *Uehara and Shimamoto*, 2004]. The permeability values for the gouge are in the range of values obtained in previous studies (10^{-17} to 10^{-21} m^2) from borehole or laboratory measurements [*Morrow et al*., 1984; *Evans et al*., 1997; *Faulkner and Rutter*, 1998; *Wibberley and Shimamoto*, 2003; *Tsutsumi et al*., 2004; *Uehara and Shimamoto*, 2004; *Boutareaud et al*., 2008; *Mizoguchi et al*., 2008; *Lockner et al*., 2009; *Tanikawa and Shimamoto*, 2009].

The permeability anisotropy for the three directions (k_h, k_H, and k_v) varies over 2 orders of magnitude for gneiss, 1 order of magnitude for phyllonite, and 3 orders of magnitude for gouge (Table 1). The permeability anisotropy for gneiss is characterized by a horizontal maximum direction of permeability k_H and a vertical minimum direction of permeability k_V. These results differ from those obtained for phyllonite for which the direction of minimal permeability is k_h while the directions k_v and k_H have similar values. Regarding the gouge, the permeability anisotropy is characterized by cores perpendicular to the fault $k_{h\text{-}b}$ having the lowest-permeability values while the cores $k_{h\text{-}a}$, k_H, and k_v have similar permeability values. The reasons for these differences are discussed later.

The variations of *P* and *S* waves velocities during confining pressure increase were measured and are characterized by a nonlinear evolution between 0 and ~100 MPa and by a linear evolution between ~100 and 190 MPa. The nonlinear evolution was interpreted by *Birch* [1960] to be due to the closure of microcracks, while the linear evolution (at $P_c > 100$ MPa) corresponds more likely to the variations of the intrinsic elastic properties of the rock. At low effective confining pressure (<70 MPa), the *P* and *S* wave first arrivals in gouge samples were difficult to pick and hence only *P* and *S* wave velocities from 70 MPa are reported in Figure 6 and in Table 1. The *P* and *S* wave velocities through cohesive rocks (gneiss and phyllonite) are similar, with V_P ranging from 5246 to 6119 m s^{-1} and V_S ranging from 3172 to 3671 m s^{-1} for effective confining pressures ranging from 70 to 190 MPa (Figure 6 and Table 1). The velocities of the *P* and *S* waves through gouge samples are slower than those for cohesive rocks, with V_P ranging from 3830 to 4636 m s^{-1} and V_S ranging from 2229 to 2618 m s^{-1}. For all samples, the V_S/V_P ratios are between 1.5 and 2. The anisotropy of the V_S and V_P differs from cohesive (gneiss and phyllonite) and noncohesive (gouge) rocks. Indeed, for the cohesive rocks, the anisotropy is characterized by a fastest k_v direction and a slowest k_h direction, while for gouge, *P* and *S* wave velocities can be considered as isotropic.

The variations of the porosity from the host rock through the damage zone and to the core zone are characterized by a damage zone having the lowest porosity and a core zone having the highest porosity (Table 1). The mean porosity of the damage zone is 1.6% and is slightly lower than the mean porosity of the host rock (2.2%). The mean porosity of the core zone is 16.9% and is significantly larger than the porosities of the host rock and the damage zone. The structural and physical properties of the studied fault differ from the classical view of faults with narrow and low permeable core zone surrounded by large and permeable damage zone [*Chester and Logan*, 1986; *Caine et al*., 1996; *Faulkner et al*., 2003]. These differences are discussed in section 6.2.

3.2.1. Pressure-Sensitivity Factor "γ"

The sensitivity of permeability to variations in confining pressures is expressed by the pressure-sensitivity factor, γ (MPa^{-1}). The term γ represents the straight line relationship in log permeability versus effective stress space. *Faulkner* [2004] showed that γ can be described by the following relationship:

$$k = k_0 \exp(-\gamma \bar{\sigma}) \tag{3}$$

where k is permeability (m^2), k_0 is a reference permeability (extrapolated back to zero pressure) (m^2), γ is the pressure-sensitivity factor (MPa^{-1}), and $\bar{\sigma}$ is the effective mean stress (mean stress minus pore fluid pressure, MPa).

Values for γ for this study are shown in Table 1 and in Figure 5. They range from 0.0015 to 0.0254 MPa^{-1}, with maximum values for gouge sample k_h, intermediate values for gneiss samples, and minimum values for phyllonite samples.

Table 2. Material Properties Used in the Hydromechanical Modeling to Simulate Fluid Pressure Build-up by Compaction

Parameters	Host Rock	Damage Zone	Core Zone
Size (m)	10	5	0.5
Porosity, Φ (−)	0.022	0.016	0.169
Permeability, κ (m^2)	4.01E-020	1.73E-021	1.91E-018
Bulk modulus, K (GPa)	48.7	47.3	28.8
Shear modulus, G (GPa)	31.7	32.2	16.6
Rock density, ρ (kg m3)	2700	2700	2700
Friction coefficient, μs (−)	0.75	0.75	0.4
Tensile strength, T (MPa)	17.5	17.5	0

3.2.2. Elastic Moduli

Based on the P and S wave velocities, the dynamic Young modulus, E_D, and Poisson ratio, v_D, can be estimated from the following relationships of isotropic materials [*Kuttruff*, 1991]. However, the E_D and v_D values must be considered with care since our rocks are transversely isotropic due to the presence of the foliation, schistosity, or shear planes. The complete characterization of the transversely isotropic elasticity tensor required five independent raypaths. This was not possible with our current sample assembly leading us to consider the rocks as isotropic.

$$E_D = \frac{\rho Vs^2(3Vp^2 - 4Vs^2)}{Vp^2 - Vs^2} \tag{4}$$

$$v_D = \frac{Vp^2 - 2Vs^2}{2(Vp^2 - Vs^2)} \tag{5}$$

where V_P is the P wave velocity, V_S is the S wave velocity, and ρ is the density of the rock. Density changes during the experiments were considered to have a negligible effect on the P and S wave velocities.

For cohesive rocks (gneiss and phyllonite), dynamic Young's moduli and Poisson ratios are similar with values ranging from 54 to 88 GPa and 0.15 to 0.27, respectively. For gouge samples, dynamic Young's moduli and Poisson ratios are between 26 to 46 GPa and 0.16 to 0.30. These values are in the range of values obtained from boreholes and laboratory measurements comprised between 10 GPa to 80 GPa and 0.1 to 0.3, respectively [*Faulkner et al*., 2006; *Wang and Ji*, 2009; *Jeppson et al*., 2010; *Blake et al*., 2013].

The values E_D and v_D allow calculation of the dynamic shear modulus (G) and bulk modulus (K) used for the numerical modeling (Table 2).

$$K = \frac{v_D}{3(1 - 2E_D)} \tag{6}$$

$$G = \frac{E_D}{2(1 + v_D)} \tag{7}$$

These elastic properties are similar to those found typically for cohesive rocks with values between 26 and 56 GPa for the dynamic bulk modulus, and between 23 and 36 GPa for the dynamic shear modulus (Figure 8). The elastic properties of gouge are half that for cohesive rocks with values between 13 and 34 GPa for the dynamic bulk modulus and between 11 and 18 GPa for the dynamic shear modulus. The dynamic bulk modulus of gouge is similar to the static bulk modulus values obtained by *Wibberley* [2002] for gouge using pore pressure volumometry.

4. Microstructural Influences on Permeability and Elastic Wave Velocity

The permeability and elastic wave velocity values obtained are strongly dependent on the type of rocks (gneiss, phyllonite, or gouge) and on the direction of the cores (Figures 5 and 6 and Table 1). The measurements show that cohesive rocks have faster P and S waves than gouge. Concerning the permeability along k_v, gneiss samples give the lowest-permeability values while phyllonite samples give the highest values. In the case of gneiss, the permeability is sensitive to the effective confining pressure (P_{eff}) while for phyllonite, P_{eff} has a low effect on the permeability. For gouge, permeability measurements give the highest values compared to gneiss and phyllonite and show a significant difference in permeability and pressure-sensitivity factors between the two core directions $k_{h\text{-}a}$ and $k_{h\text{-}b}$.

All these results show that the hydraulic and elastic properties of the three studied rock types are not controlled by the same microstructures. The origin of the microstructures controlling the hydraulic and elastic properties of rocks can be sedimentary, such as bedding [*Yang and Aplin*, 2007; *Chen et al*., 2009; *Armitage et al*., 2011], metamorphic, such as foliation or cleavage [*Faulkner and Rutter*, 1998; *Leclère et al*., 2012b], or tectonic such

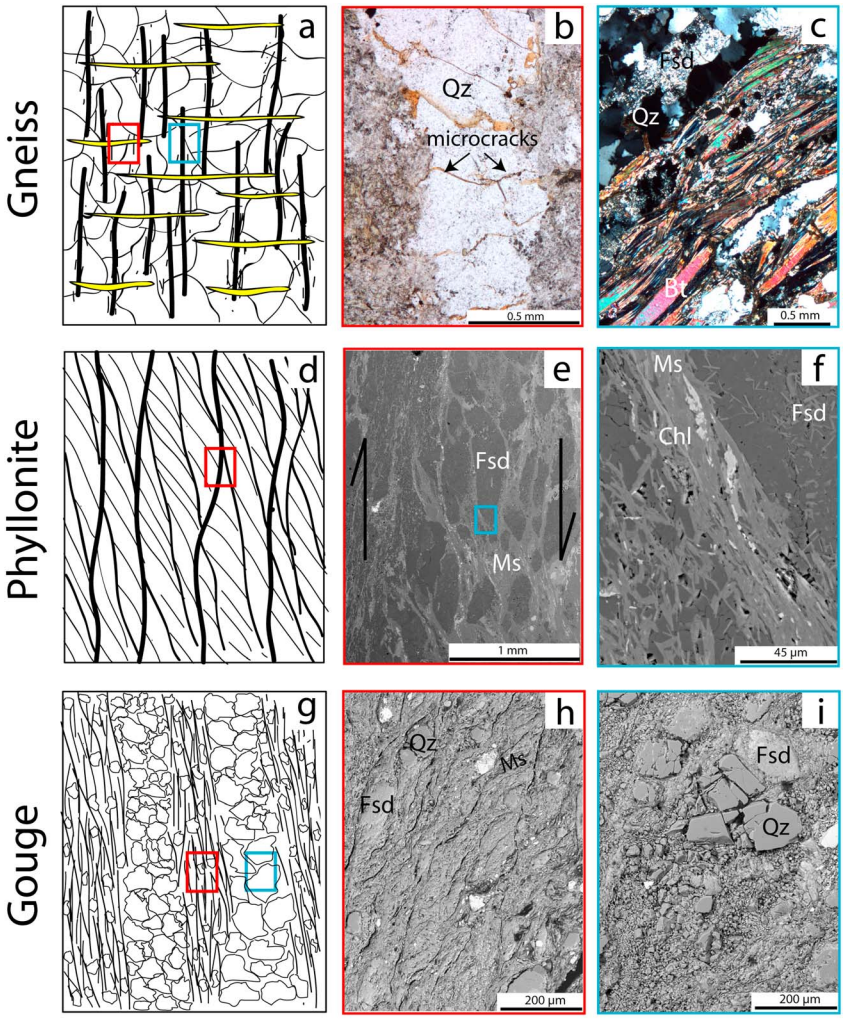

Figure 7. Microstructures controlling the permeability and the *P* and *S* wave velocities. (a) Sketch of gneiss showing the microcracks (horizontal yellow lines) controlling the permeability and the foliation (vertical black lines) controlling the *P* and *S* wave anisotropy. (b) Microcracks crosscutting a quartz aggregate in gneiss (optical microscope photomicrograph). (c) Gneiss foliation (optical photomicrograph). (d) Sketch of phyllonite showing S-C structures controlling the permeability and the *P* and *S* wave anisotropy. (e) Phyllosilicate-rich layers in phyllonite (scanning electron microscope (SEM) image). (f) Phyllosilicate-rich layers along shear surfaces in phyllonite (SEM image). (g) Sketch of gouge showing low-permeability fine-grained phyllosilicates-rich layers and high-permeability coarse-grained quartz-feldspar layers. (h) Low-permeability fine-grained phyllosilicate-rich layers (SEM image). (i) Coarse-grained quartz-feldspar layers in gouge (SEM image). Bt: Biotite; Ms: Muscovite; Chl: Chlorite; Qz: Quartz; and Fsd: Feldspar.

as microcracks [*Morrow et al.*, 1994; *Heikamp and Nover*, 2003; *Mitchell and Faulkner*, 2008]. The presence of bedding, foliation or cleavage surfaces, and microcracks can be responsible for the anisotropy of permeability and elastic properties [*Faulkner and Armitage*, 2013]. In the direction parallel to foliation, cleavage, or microcrack networks, fluid flow can be channelized while in the direction perpendicular to bedding, foliation, or cleavage, fluid-flow and elastic waves are slowered.

For gneiss samples, the direction of the lowest permeability is vertical and that of the highest permeability is horizontal, both directions being parallel to the foliation (Table 1). These results are inconsistent with a control of the anisotropy of permeability by the foliation. The nature of the rocks also precludes a control by sedimentary bedding since the high degree of metamorphism erased all primary sedimentary or volcano-sedimentary structures. Microcracks oriented perpendicularly to the foliation planes, and crosscutting quartz and feldspar ribbons (Figures 7a and 7b) appear to be a possible explanation for the anisotropy. These microcracks could correspond to tension fractures formed during the Alpine

compressional tectonic events. They could also result from stress release during removal of the overburden by erosion and/or uplift. A detailed study of these microcracks, which could help determining their origin, was not carried out during this study. A control of the permeability by microcracks was already proposed by *Morrow et al.* [1994] and *Heikamp and Nover* [2003] for gneiss samples from KTB and Kola boreholes. These authors further showed a decrease of permeability of gneisses during the increase of the confining pressure. The influence of microcracks on permeability anisotropy is supported by the high values of the pressure-sensitivity factor γ for gneiss, as microcrack closure is very sensitive to pressure (Table 1 and Figure 5).

The anisotropy of the elastic wave velocities for gneiss is characterized by the slowest direction perpendicular to the foliation planes (k_h) and the fastest direction parallel to the foliation planes and perpendicular to the microcracks (k_v). The anisotropy of the elastic wave velocities appears to be dominated by the minerals constituting the foliation and not affected by microcracks although they strongly influence the permeability anisotropy (Figures 7a–7c). The lack of influence of microcracks on the elastic wave velocities can be explained by the fact that a microcrack closed for elastic wave transmission can be an open microcrack for fluid flow [*Benson et al.*, 2006]. Indeed, even a partial closure of microcracks allows elastic waves to cross the microcracks, whereas a total closure of microcracks is required to impede the fluid flow.

In the case of phyllonite, the lowest permeabilities and the slowest elastic wave velocities are obtained in the k_h direction, that is in a direction perpendicular to the phyllosilicate-rich shear surfaces (C). Conversely, the highest permeabilities and the fastest elastic wave velocities are obtained in the k_v direction, that is in a direction parallel to the S-C intersection (Figure 3d). The low pressure-sensitivity factors for the phyllonite suggest that microcracks have a low influence on the anisotropy of permeability. These results show that the S-C structure influences the permeability anisotropy and elastic wave velocities. Petrographical observations show that fluid flow is likely controlled by micropores localized between platy phyllosilicate minerals filling S-C planes (Figures 7d–7f) as previously discussed by *Faulkner and Rutter* [1998], *Wibberley and Shimamoto* [2003], *Uehara and Shimamoto* [2004], and *Leclère et al.* [2012b].

The results for the gouge can be divided into two categories. The first category corresponds to cores $k_{h\text{-}a}$, $k_{H\ a\text{-}b}$, and core $k_{v\ a\text{-}b}$ showing isotropic permeabilities and isotropic elastic wave velocities (Figures 5 and 6). The permeability of these cores is characterized by a low sensitivity to the increase of effective confining pressure as shown by low pressure-sensitivity factors γ (Table 1 and Figure 5). For these samples, pore closure and permeability reduction during the increase of effective confining stress appear to be negligible. The low deformation of the copper jacket after the experiment is in agreement with a low pore closure and a low volume reduction during the increase of the effective confining stress up to 190 MPa. The second category corresponds to the core $k_{h\text{-}b}$ showing a contrasting permeability behavior characterized by a low-permeability and a high pressure-sensitivity factors.

Previous experimental analyses show that the gouge permeabilities can be sorted in two end-members:

1. Clay-rich gouge having low permeabilities (10^{-18} to 10^{-21} m^2) and high pressure-sensitivity factors γ [*Morrow et al.*, 1984; *Faulkner and Rutter*, 1998; *Wibberley and Shimamoto*, 2003; *Uehara and Shimamoto*, 2004; *Boutareaud et al.*, 2008; *Crawford et al.*, 2008; *Ikari et al.*, 2009].
2. Granitic or coarse-grained quartz-feldspar-rich gouge having high permeabilities (10^{-14} to 10^{-17} m^2) and low pressure-sensitivity factors γ [*Zhang et al.*, 1999, 2001; *Crawford et al.*, 2008; *Behnsen and Faulkner*, 2011].

The analyzed gouges are composed of alternations of fine-grained phyllosilicate-rich layers and coarse-grained quartz-feldspar layers (Figures 3e and 7g–7i). The phyllosilicate-rich layers are composed of phyllosilicates which define S-C planes and which are distributed between quartz-feldspar grains (Figure 7h). Coarse-grained layers are composed of quartz and feldspars clasts delimiting pores (Figure 7i). The porosity network of gouge is characterized by equant pores in the quartz-feldspar layers that are not sensitive to compaction and by micropores between phyllosilicates minerals that are sensitive to compaction. The high isotropic permeability values (~10^{-17} m^2) and the low pressure-sensitivity factors γ obtained for cores $k_{H\ a\text{-}b}$, $k_{v\ a\text{-}b}$, and $k_{h\text{-}a}$ show that the permeability is mainly controlled by connected pores located between coarse quartz and feldspar clasts (Figures 7g–7i). Conversely, the low-permeability and the high pressure-sensitivity factors γ of the core $k_{h\text{-}b}$ show that the permeability is mainly controlled by micropores located between phyllosilicates (Figures 7g–7h). The results obtained for the core $k_{h\text{-}b}$ are in agreement with *Faulkner and Rutter* [1998] who also showed that the cores perpendicularly oriented to the foliation have the lowest permeabilities and the

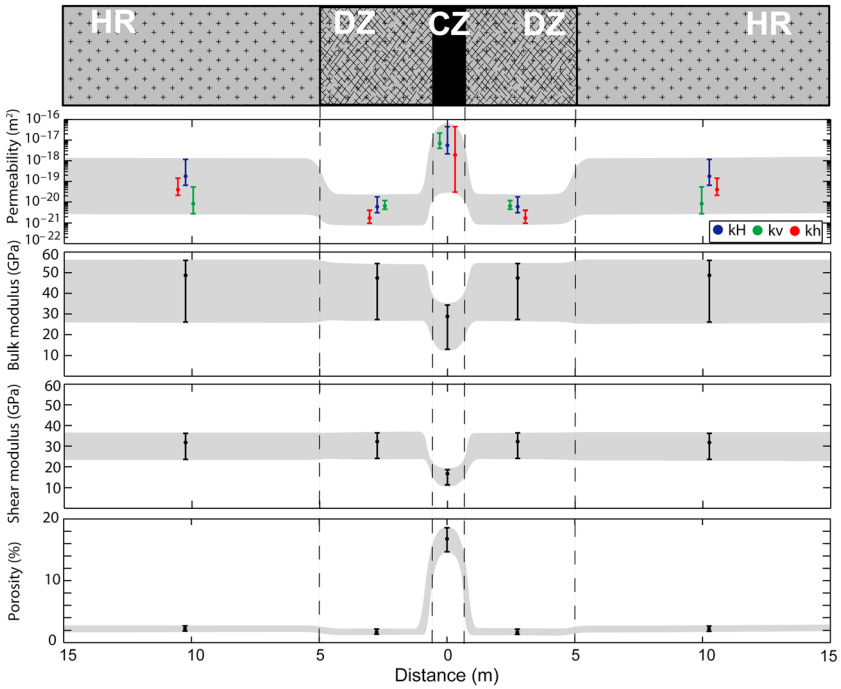

Figure 8. Horizontal profile across the fault zone of the hydraulic and elastic properties values measured in laboratory. Verticals bars correspond to the range of values. Dots correspond to the expected hydraulic and elastic properties at the hypocentral depths of the 2003–2004 Ubaye seismic swarm. HR: Host rock; DZ: Damage zone; and CZ: Core zone.

highest pressure-sensitivity factors γ. The difference in permeability between cores $k_{h\text{-}a}$ and $k_{h\text{-}b}$ is thus controlled by the presence of fine-grained phyllosilicate-rich layers.

The similarity between elastic wave velocities measured in samples $k_{H\ a\text{-}b}$, $k_{v\ a\text{-}b}$, and $k_{h\text{-}a}$ shows that coarse-grained quartz-feldspar layers do not develop any anisotropy in *P* and *S* wave velocities. Furthermore, the similarity between the *P* and *S* wave velocities between for the two samples $k_{h\text{-}a}$ and $k_{h\text{-}b}$ shows that the propagation of the elastic waves was not sensitive to the fine-grained phyllosilicate layers. The propagation of the elastic waves appears to be controlled more by clast contacts than by phyllosilicates along S-C structures. These results are in contrast with those obtained for phyllonite where S-C structures influence *P* and *S* waves. This difference can be explained by millimeter thick S-C planes mainly composed of phyllosilicates in phyllonite (Figure 7e), while for gouge, phyllosilicates are pinched out between quartz and feldspars clasts along fine-grained phyllosilicate-rich layers (Figure 7h). The presence of phyllosilicates between clasts helps reducing the pore throat radius and can explain the reduction of permeability observed in cores $k_{h\text{-}b}$ and also reported in other clay-bearing rocks by *Armitage et al.* [2011]. However, the phyllosilicates are not continuous enough to induce any anisotropy in the elastic wave propagation.

The observation showing that *P* and *S* wave velocities are slower in gouges than in phyllonites or in gneisses is also in agreement with elastic waves controlled by grain contacts. Indeed, gouges are more porous than phyllonites and gneisses, and it is thus more difficult for elastic waves to bypass pores in gouge than in phyllonites and gneisses. The high-porosity values measured for gouge are in the range of values determined by *Crawford et al.* [2008] for gouge rich in quartz having a grain size between 63 and 125 μm, by *Boutareaud et al.* [2008] for natural gouge from the Usukidani fault, and by *Tanikawa and Shimamoto* [2009] for gouge samples collected along the Chelungpu fault.

Figure 8 summarizes the hydraulic and elastic properties of the studied fault where vertical bars correspond to the values measured over the pressure range, and dots correspond to the expected, hydraulic, and elastic properties at the 7 km mean hypocentral depth of the 2003–2004 Ubaye seismic swarm. Figure 8 shows that hydraulic and elastic properties vary laterally across the studied fault and are characterized by (1) a core zone having the highest values of permeability and porosity and the lowest elastic properties controlled by pores and clast contacts, and (2) a low-porosity damage zone having the lowest values of permeability controlled by S-C structures.

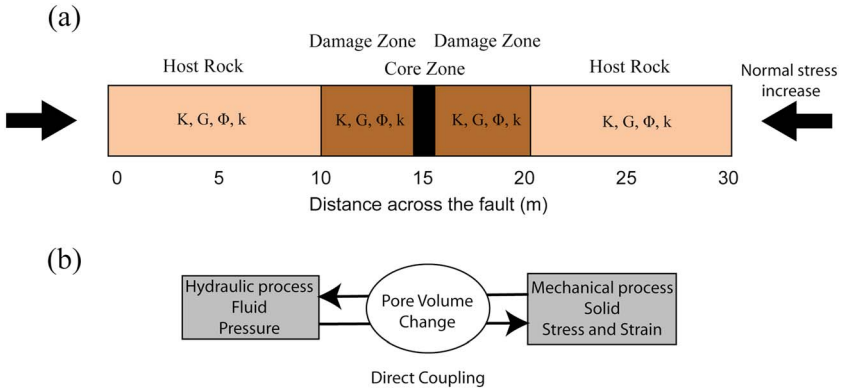

Figure 9. Setup of the hydromechanical modeling: (a) Fault model geometry composed of vertical elements sealed by a horizontal impermeable caprock. Model size, hydraulic, and elastic properties are defined from field and laboratory measurements. (b) Illustration of the direct hydromechanical couplings in geological media through pore volume interactions.

5. Hydromechanical Modeling Combining Field Geological Analysis and Laboratory Measurements

5.1. Numerical Method and Basic Assumptions

Coupled hydromechanical modeling was used to investigate the interactions between deformation and fluid pressure during elastic compaction of the studied fault. The model is based on the structure and physical properties of the analyzed fault and on the characteristics of the 2003–2004 Ubaye swarm. The objectives are (1) to analyze how fluid overpressures can develop, can be maintained, and can diffuse in a compartmented, heterogeneous fault zone subjected to a mechanical shortening induced by an instantaneous compressive loading event. This loading is constrained from static Coulomb failure stress (ΔCFS) and dynamic Coulomb failure stress (ΔCFS(t)) changes occurring after large earthquake or during seismic swarm activity; (2) to perform a parametric study in order to assess the sensitivity of fluid overpressures to the variations in hydraulic and elastic properties in the fault, and the size of the damage zone, (3) to determine if elastic compaction is a viable mechanism to trigger seismic swarm activity such as observed during the 2003–2004 Ubaye seismic swarm.

In the model, the anastomosed fault zone observed in the field (Figure 2) is too complex to be modeled. It is therefore replaced by one of its branches consisting of a core zone surrounded by two damage zones, the damage zones being flanked by the intact protolith. The fault zone is thus represented as a set of five juxtaposed layers whose widths are based on field measurements. A central 0.5 m thick core zone (CZ) is surrounded by two 5 m thick damage zones (DZ) which are flanked by a 10 m thick host rock (HR) (Figure 9a). Within each fault constitutive layer, the hydraulic and physical properties measured in the laboratory and represented by dots in Figure 8 are applied (Table 2). The model used here is a 1-D model oriented perpendicular to the fault strike. The one-dimensional configuration is representative of the hydromechanical processes occurring in the fault zone because most of the deformation and fluid flow induced by normal stress variations occur perpendicularly to the fault zone boundaries. Fluid flow considered as predominantly perpendicular to the fault zone is justified by the length scales involved. Despite the fact that the permeability of core k_h from the damage zone is 3 orders of magnitude lower than the permeability of core k_H from the gouge zone, the fluid-flow path length perpendicular to the fault will be much less than that parallel to the fault. In the case of a 0.5 m thick fault core zone, as measured in the field, fluid flow will occur predominantly in the direction perpendicular to the fault zone, provided that the fault is longer than 500 m. Given the fact that the 2003–2004 Ubaye swarm is aligned along a 9 km long rupture zone [*Jenatton et al.*, 2007], fluid flow likely occurred predominantly in the direction perpendicular to the fault. In the model, vertical fluid flow is not taken into account. Indeed, the presence of the 1–2 km thick post-Variscan sedimentary pile (sedimentary cover and sedimentary nappes) above the hypocentral region of the 2003–2004 Ubaye seismic swarm prevents or restricts upward fluid escape [*Leclère et al.*, 2012a] (Figure 1).

The explicit finite difference code, FLAC^{3D} (Fast Lagrangian Analysis of Continua in 3-D) [*Itasca Consulting Group*, 2006], was employed to model hydromechanical processes occurring in the fault studied here.

FLAC^{3D} allows simulation of the interactions between deformation and fluid flow in porous media and has been already used successfully in the modeling of faulting in different geological and tectonic contexts [*Sheldon and Ord*, 2005; *Zhang et al*., 2008; *Ford et al*., 2009; *Cappa*, 2009, 2011]. Although the model allows elastic-plastic deformation to be taken into account, only the elastic deformation (ε_{ij}^{e}) is considered here since the fault is not in a critical state inducing plastic deformation.

The elastic strain (ε_{ij}^{e}) is computed using Hooke's equation

$$\varepsilon^{e_{ij}} = \frac{\sigma_{ij}}{2G} - \left(\frac{1}{6G} - \frac{1}{9K}\right)\delta_{ij}(\sigma_{11} + \sigma_{22} + \sigma_{33}) + \frac{\alpha}{3K}\delta_{ij}p_f \tag{8}$$

where σ_{ij} is the total stress tensor, δ_{ij} is the Kronecker delta, K and G are the bulk modulus and the shear modulus of the drained elastic solid, Pf is the fluid pressure, and α is the Biot's coefficient. K can be expressed as a function of the fluid bulk modulus (K_f fixed at 2 GPa for water), the undrained bulk modulus (K_u), and the porosity (ϕ) by assuming incompressible solid constituents [*Detournay and Cheng*, 1993]. Note that although the solid is assumed to be incompressible, the voids are able to change in volume, since fluid can enter or leave the skeleton.

$$K = K_u - \frac{K_f}{\phi} \tag{9}$$

In the FLAC code, changes of fluid volume are related to changes in fluid pressure (Pf) and mechanical volumetric strain ($\Delta V/V$). During a simulation, hydraulic and mechanical behaviors are coupled in two ways (Figure 9b): (1) changes in fluid pressure cause changes in effective stress ($\sigma' = \sigma - Pf$, where σ is the total stress) affecting the deformation of the solid and (2) fluid pressure changes react to mechanical volume changes (i.e., volumetric strain, $\Delta V/V = \varepsilon_1 + \varepsilon_2 + \varepsilon_3$, where ε_1, ε_2, and ε_3 are principal strains) by changing its fluid pressure according to

$$\Delta P = \frac{-K_f}{\phi} \cdot \frac{\Delta V}{V} \tag{10}$$

where V is the initial volume, and ΔV is the volume change due to deformation. For instance, compaction (ΔV negative) is due to a decrease in fluid pressure or an increase of the effective pressure, and dilation (ΔV positive) is due to an increase in fluid pressure or a decrease of the effective pressure. Volumetric changes associated with compaction or dilation will also have an effect on pore fluid pressure resulting in an increase of pore fluid pressure during compaction and a decrease of pore fluid pressure during dilation. In the model, fluid transport is governed by the diffusion equation derived from the continuity of fluid mass and the Darcy's law

$$\nabla \cdot \left[\frac{k_{ij}}{\eta}\left(\nabla P + \rho_f g \nabla x_{ij}\right)\right] = S\frac{\partial P}{\partial t} \tag{11}$$

where k_{ij} is permeability, η is fluid viscosity (fixed at 10^{-3} Pa s for water), x_{ij} reflects the position of a material point in the grid, g is gravity, ρ_f is fluid density (1000 kg/m^3 for water), t is the time, and S is the specific storativity expressed as in *Segall and Rice* [1995] by $S = \phi(\beta_s + \beta_f)$ as a function of the porosity, the pore compressibility β_s, and the fluid compressibility β_f. Therefore, fluid flow is transient (i.e., not instantaneous) and is driven by gradients in fluid pressure and variations in permeability and porosity. At the starting time t_0, the model is fully saturated with water, and a constant hydrostatic fluid pressure and lithostatic stress are imposed on the lateral boundaries. The boundaries of the model are open to fluid flow, and the initial volume of fluid is thus not kept constant during the modeling. The modeling procedure consists of two steps: (1) the model was first run to reach a steady state having the hydrostatic fluid pressure and the lithostatic stress at a 7 km depth before external loading is applied; (2) once the steady state initial conditions are set, a uniform increase in horizontal stress is instantaneously applied perpendicularly to the lateral boundaries and the evolution of the fluid pressure in the fault zone through time and space is investigated. The value of normal stress increase is equal to 1 MPa and then extended between 0.1 MPa and 10 MPa for the sensitivity tests corresponding to the range of Coulomb failure stress (ΔCFS) and dynamic Coulomb failure stress (ΔCFS(t)) changes occurring after a large earthquake or during seismic swarm activity [*King et al*., 1994; *Belardinelli et al*., 1999; *Stein*, 1999; *Kilb et al*., 2000; *Aoyama et al*., 2002; *Terakawa et al*., 2010; *Yukutake et al*., 2011].

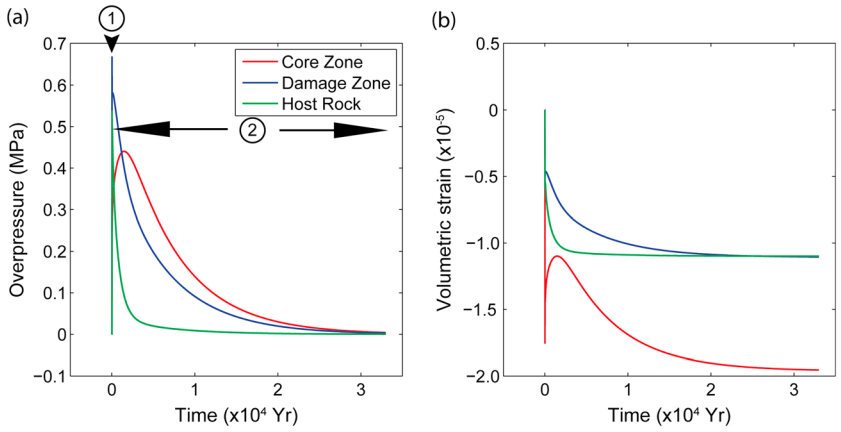

Figure 10. Results of the hydromechanical modeling for a mechanical stressing of 1 MPa. (a) Evolution of the fluid overpressures and (b) volumetric strain in the host rock, damage zone, and core zone over time. 1: Undrained response, 2: Drained response. Control points are located at the center of each zone.

5.2. Modeling Results and Sensitivity Analysis

5.2.1. General Features of the Fluid Pressure Evolution

The evolution of the fluid overpressure and volumetric strain over time for the host rock, damage zone, and core zone is presented in Figure 10. The origin time t_0 corresponds to the instantaneous increase of normal stress on the fault. Results show that the fluid overpressures develop instantaneously in each fault compartment after the stress change and then progressively decrease over time. Maximum overpressure values (~0.68 MPa) are produced in the damage zone, and minimum values (~0.35 MPa) are produced in the core zone. The maximum value of ~0.68 MPa is much lower than the overpressured values between 20 and 55 MPa estimated by *Leclère et al*. [2013] for the 2003–2004 Ubaye seismic swarm. The difference can be explained by the fact that, in this study, elastic deformation only is taken into account since the fault does not reach the yield envelope, whereas *Leclère et al*. [2013] explained the development of fluid overpressured by creep compaction involving plastic deformation. Creep compaction induces a higher pore compaction than does elastic deformation, hence explaining the differences of fluid overpressures between the present model and the analysis of *Leclère et al*. [2013]. The maximum fluid overpressure value estimated here thus corresponds to the minimal fluid overpressure than can be developed in the fault zone since plastic deformation is not taken into account in this study.

The evolution of fluid pressure in time shows two responses: (1) the undrained response (arrow numbered 1 in Figure 10a) that corresponds to the rapid development of the maximum peak of fluid overpressures in response to the mechanical stressing; (2) the drained response (arrow numbered 2 in Figure 10a) that corresponds to the diffusion of the fluid pressures over time across the fault zone elements.

The comparison between the evolution of fluid overpressures and volumetric strain over time (Figure 10) shows that the increase in fluid pressures during the undrained response is associated with a contraction (i.e., negative volumetric strain) in all fault elements. Then, during the drained response, deformation and fluid flow are controlled by the pressure differences between the different parts of the fault.

5.2.2. Sensitivity Tests for the Undrained Response

A series of sensitivity tests was performed for the undrained response, and it shows how the development of fluid overpressures in the host rock, damage zone, and core zone is influenced by the elastic properties (bulk and shear moduli), the porosity, and the loading (Figure 11). For this parametric analysis, only the tested parameter was modified with a same value for the host rock, damage zone, and core zone while the other parameters were kept constant.

In Figure 11a, a decrease of the bulk and shear moduli induces an increase of compaction strain (i.e., negative volumetric strain) and an increase of the fluid overpressures both in the fault and the host rock. The development of fluid overpressures is more efficient in the damage zone and in the host rock than in the core zone, although the damage zone and host rock are less deformed than the core. This difference can

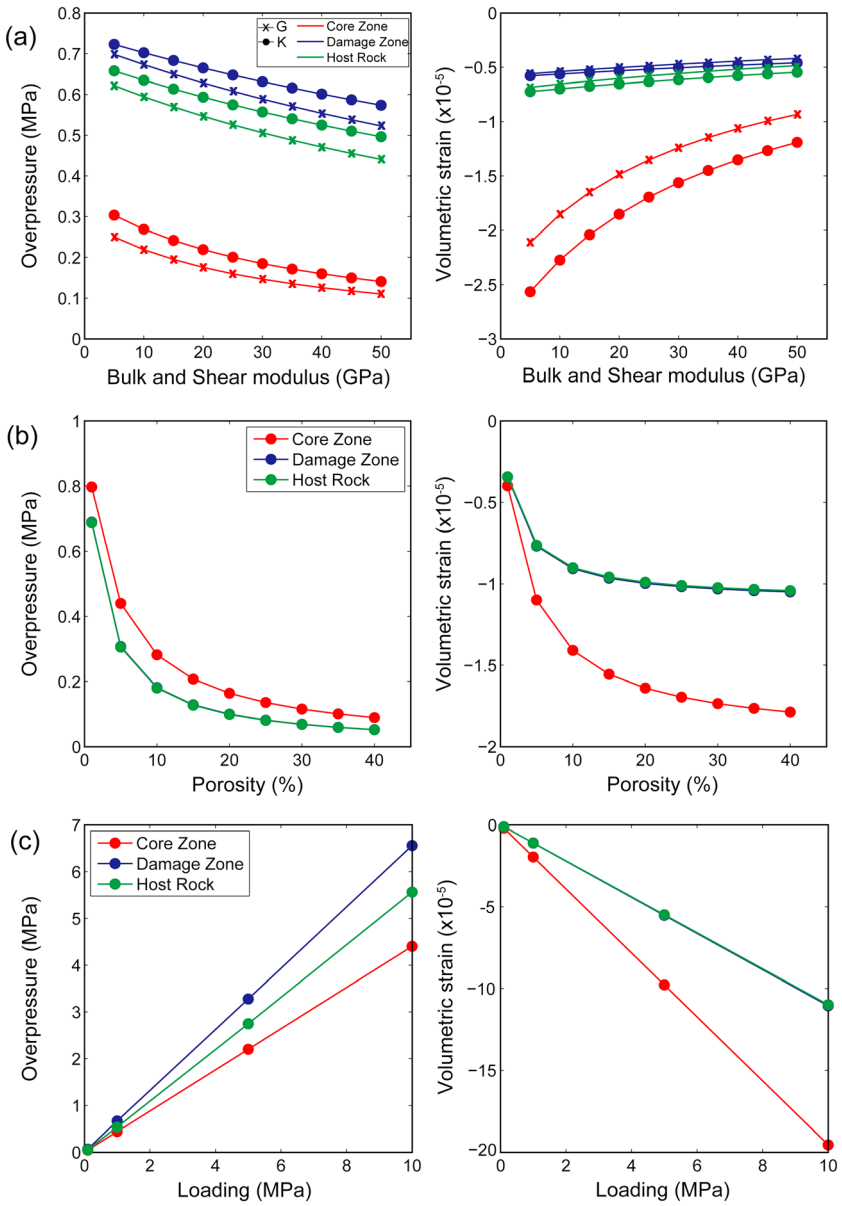

Figure 11. Sensitivity tests of the fault undrained response illustrating the influence of changes in (a) elastic properties, (b) porosity, and (c) loading on the development of fluid overpressures and on the volumetric strain in the fault. Concerning the curves of Figure 11b (both sides) and Figure 11c (right side), the values computed for host rock samples are very close to those computed for damage zone samples, thus accounting for overlapping plots.

be explained by the porosity contrast between the gouge and the cohesive rocks. Indeed, the development of fluid pressure is more efficient in low-porosity rocks than in high-porosity rocks.

In Figure 11b, the tested porosity values range from low-porosity rocks such as those measured in this study (1%) to high-porosity rocks (40%) such as those measured in quartz-rich gouges [*Crawford et al.*, 2008]. The increase of the porosity induces an increase of the volumetric strain which is not associated with an increase of the fluid overpressures. This behavior can be also explained by a development of fluid pressure being more effective in low-porosity rocks even if the associated volumetric strain is lower than for high-porosity rocks.

Lastly, Figure 11c shows that the peak of fluid overpressure and the associated volumetric strain are proportional to the loading values according to elasticity. However, it is important to note that the maximum peaks of fluid overpressures reached during the undrained response remain always lower than the values of normal stress increase (i.e., loading).

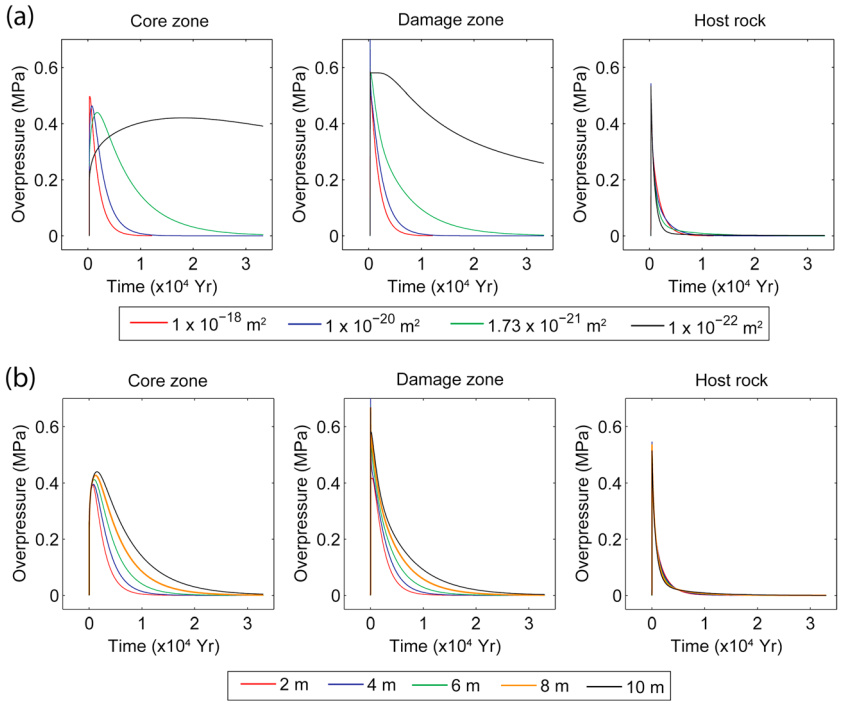

Figure 12. Sensitivity tests of the fault drained response illustrating the influence of change in (a) permeability and (b) width of damage zone on the fluid overpressures from the core through the damage zone to the host rock.

5.2.3. Sensitivity Tests for the Drained Response

The parametric tests performed for the drained response show that the evolution of the fluid overpressures across the fault zone is sensitive to the permeability and the thickness of the damage zone (Figure 12).

The tested permeability values vary over 2 orders of magnitude around the mean measured permeability value (10^{-20} m^2) of the damage zone (Figure 8). The permeability value of 10^{-22} m^2 is an extreme value and would represent a very low permeability cemented damage zone. The maintenance of the fluid overpressures in the damage zone and in the core zone is highly sensitive to the damage-zone permeability compared to the host rock permeability (Figure 12a). A reduction of the damage-zone permeability from 10^{-21} to 10^{-22} m^2 allows a much longer maintenance of the fluid overpressures in the core zone and in the damage zone compared to a permeability reduction from 10^{-18} to 10^{-21} m^2. A damage zone permeability of 10^{-21} m^2 appears as a threshold value for the studied fault allowing long-term maintenance of fluid overpressures in the core zone. Figure 12b shows the influence of the damage-zone thickness on the evolution of fluid overpressures in the fault elements. The fluid overpressure in the host rock is hardly affected by the change in damage-zone thickness. However, the increase of the damage-zone thickness maintains a longer-term fluid overpressure both in the damage zone and in the core zone. The increase of the damage-zone thickness also induces the development of higher peaks of fluid overpressures in the core zone.

6. Implications for Earthquake and Fault Mechanics

This section is composed of three subsections. Subsection 6.1 presents the evolution of the fluid overpressures in the studied fault based on the results of the hydromechanical modeling. Subsection 6.2 discusses then the structures of the studied fault and the development of its hydraulic and elastic heterogeneities. Lastly, subsection 6.3 discusses the implications of development and maintenance of fluid overpressures by elastic compaction for seismic swarm events.

6.1. Evolution of Fluid Overpressures in the Studied Fault Zone

At the initial conditions, fluid pressure is at the hydrostatic equilibrium (Figure 10 and step 1 in Figure 13). During the mechanical stressing, the host rock, the damage zone, and the core zone compact in response to the increase in normal stress (Figure 10b). The elastic compaction of the fault induces the development

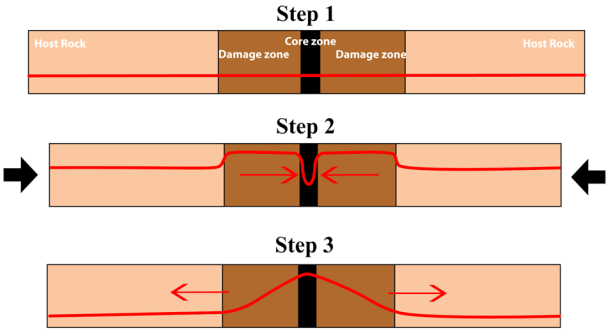

Figure 13. Conceptual model of the evolution of fluid overpressures due to elastic compaction over time (steps 1 to 3) based on the hydromechanical modeling results. The red line represents the evolution of fluid pressure across the fault zone.

of the highest fluid overpressure values in the damage zone and the lowest fluid overpressure values in the core zone due to the porosity contrast (Figure 10b). At step 2 in Figure 13, which corresponds to the peak of fluid overpressures, fluid flow is driven by the highest pore pressure gradient between the damage zone and the core zone. The migration of the fluid overpressures from the damage zone to the core zone is evidenced by an increase of the fluid overpressures in the core zone and by a decrease at the same time in the damage zone (Figure 10a). The migration of fluid pressure is also seen in Figure 10b by dilation in the fault core zone (pore pressure increase) immediately after the initiation of the undrained response while damage zone continues to compact (pore pressure decrease) at the same time. At step 3 in Figure 13, the fluid overpressures in the core zone equal the fluid overpressures in the damage zone. The highest gradient of fluid overpressures is now from the core zone to the host rock. Fluid flow thus diffuses outside the fault zone as shown by a decrease of the fluid overpressures in core zone and by a change of volumetric strain from dilation to compaction in the core zone (Figure 10). The maintenance of fluid overpressures in the fault core zone during step 3 is then totally controlled by the thickness and the permeability of the damage zone. For the ranges of damage zone permeability and thickness values tested here, fluid overpressures are maintained in the core zone for long-lasting time periods (of the order of 10^3 to 10^4 years).

6.2. Structure of Faults Able to Develop and Maintain Fluid Overpressures During Fault Compaction

This study shows that elastic compaction is a viable mechanism to account for fluid pressure buildup and that the development and maintenance of fluid pressure are strongly controlled by the heterogeneous hydraulic and elastic properties of the fault zone. The internal structure of fault zones is typically divided into two zones: the core zone and the damage zone. The development of these zones is achieved during the accumulation of deformation and the mineralogical transformations through time. Depending on the P-T conditions of deformation, the lithologies and the architecture of fault zones differ [*Sibson*, 1977]. In quartzo-feldspathic rocks, three categories of rocks are commonly described with depth: mylonites above 300°C (~10 km), cataclasites between ~10 and ~5 km, and finally incohesive gouge and breccias at shallow depths.

The presence of phyllonite in the damage zone of the studied fault and gouge in the core zone indicates that faulting occurred successively from deep to shallow depths during the exhumation of the Argentera massif in the last 22 Ma [*Corsini et al.*, 2004; *Sanchez et al.*, 2011b]. The mylonitization of gneiss at depth (>10 km) allowed the development of S-C structures rich in phyllosilicates that are responsible for the low-permeability damage zone in the direction perpendicular to the fault trend. At shallow depths (<5 km), the microfracturing of inherited phyllonite in the core zone induced the development of fine-grained phyllosilicate-rich layers and coarse-grained quartz and feldspar layers having lower elastic properties and higher permeabilities and porosities than the damage zone. The development of contrasting microstructures during the fault exhumation history is thus responsible for the measured hydraulic and elastic heterogeneities across the fault.

However, the hydraulic properties of the studied fault differ from those typically reported in classical models referring to a low-permeability fault core surrounded by high-permeability damage zones relative to the host rock [*Caine et al.*, 1996; *Evans et al.*, 1997; *Lockner et al.*, 2009]. This difference can be explained by brittle deformation overprinting and reactivating plastic S-C structures along narrow layer corresponding to the fault core gouge (Figure 3a). The reactivation of S-C structures by cataclastic flow during the brittle-plastic transition microfractured cohesive phyllonite and formed incohesive gouge. The preferential sliding along S-C structures can be explained by the presence of low-friction phyllosilicates as measured in laboratory

where slip occurring parallel to the foliation has extremely low friction coefficients ($\mu = 0.2–0.4$) [*Collettini et al.*, 2009a; *Mariani et al.*, 2006; *Moore and Lockner*, 2004; *Numelin et al.*, 2007; *Behnsen and Faulkner*, 2012]. The reactivation of weak mylonitic foliation favored the localization of deformation toward narrow fault gouge layers and prevented fractures from developing in the damage zone. This model of fault development is different from those proposed by *Faulkner et al.* [2011] for classical faults where fault localization is controlled by the growth and coalescence of cracks explaining the highly fractured damage zone. The reactivation of inherited weak structures such as foliation is thus responsible for the contrasted physical properties measured between classical fault and the studied fault here. *Walker et al.* [2013] also reported a high-porosity and high-permeability fault core zone in faults developed in basaltic rocks. These authors explained the development and maintenance of high porosities and high permeabilities by high pore fluid pressures and low effective stresses. In the case of the studied fault, the development of porosity in the core zone cannot be explained by hydrofracturing, as attested by the absence of dilation breccia. However, dilatancy as showed by *Marone et al.* [1990] during shear experiments in simulated fault gouge may have increased the porosity. As discussed by *Walker et al.* [2013], high porosities and permeabilities may then have been sustained by high pore fluid pressures since the fault core zone acted as a preferential fluid pathway.

Because of its low damage-zone permeability and porosity compared to the core zone, the studied fault is an example of fault architecture that allows the development and maintenance of fluid overpressures by elastic compaction. Among large-scale crustal faults, the Median Tectonic Line (MTL) in SW Japan exposes a similar fault structure with mylonite/cataclasite/phyllonite/breccia/gouge across the fault zone [*Jefferies et al.*, 2006]. This sequence of fault rock also results from a long and complex history of deformation, at depths ranging from middle crust to shallow crust [*Wibberley and Shimamoto*, 2003; *Jefferies et al.*, 2006]. The core zone of the MTL is composed of incohesive rocks surrounded by low-permeability rocks acting as hydraulic barriers [*Wibberley and Shimamoto*, 2003; *Uehara and Shimamoto*, 2004]. Based on the results obtained in this study, a preliminary analysis suggests that the MTL may be also subject to the development and to maintenance of fluid overpressures by elastic compaction.

6.3. Elastic Compaction, a Viable Mechanism to Trigger Earthquake Swarms?

Earthquake swarms are atypical seismic events characterized by intense microseismic activities that can last for several days to several years. Many models have attempted to explain the origin of seismic swarms. Fluid pressure diffusion from surface [*Hainzl et al.*, 2006; *Rigot et al.*, 2008] or from depth [*Miller et al.*, 2004; *Cappa et al.*, 2009] has often been reported to explain the triggering of seismic swarms. Aseismic creep and compaction creep have been also proposed to explain the migration of seismic activity [*Bourouis and Bernard*, 2007; *Lohman and McGuire*, 2007; *Wicks et al.*, 2011; *Leclère et al.*, 2013], while Coulomb stress transfer and stress relaxation have been invoked to explain seismic swarms occurring after large to moderate earthquakes [*Yukutake et al.*, 2011; *Chouliaras et al.*, 2013]. This study shows that these models are not independent but can act in concert. Indeed, the hydromechanical analysis conducted here shows that the Coulomb stress transfer following an earthquake is capable of elastically compacting faults and developing fluid pressure which can then migrate through the fault zone and trigger earthquakes. In the case of the Hakone volcano swarm in Japan, *Yukutake et al.* [2011] proposed that the local stress changes generated by the initial events of the swarm might be responsible for triggering the later burst-like events. At Hakone, the magnitude of the stress changes ΔCFS is in the range of 0.01 and 0.02 MPa. Based on our numerical analysis, the low stress changes of 0.01 and 0.02 MPa might induce low-pore fluid pressure changes in the volcanic channels surrounded by low-permeability rocks. Low-pore fluid pressure changes may thus trigger earthquakes along faults close to the critical state. From the analysis of the 2003–2004 Ubaye swarm, *Leclère et al.* [2013] also inferred that creep compaction locally developed pore fluid pressure which then diffused through the fault zone and triggered seismicity. Other studies (e.g., *Bourouis and Bernard* [2007] or *Cornet et al.* [1997]) also proposed aseismic creep as a viable mechanism for triggering earthquake swarms. *Bourouis and Bernard* [2007] showed that, during fluid injections in the geothermal site of Soultz-sous-Forêts (France), the increase of pore fluid pressure up to 10 MPa induced microseismic swarm activity. However, the triggering of microseismic activity requires a stabilization mechanism to prevent rupture propagation and triggering of a large earthquake. Based on the analysis of multiplets, *Bourouis and Bernard* [2007] proposed that the microseismic activity is triggered by the seismic slip of asperities driven by the aseismic creep of the surrounding fault zone. Indeed, the development and maintenance of pore fluid pressure triggered aseismic

creep concentrating stress on asperities, eventually leading to microseismic slip. Dilatant strengthening has been also suggested as a mechanism able to inhibit the onset of instability during the period of accelerating slip [*Lockner and Byerlee*, 1994; *Yamashita*, 1999; *Segall et al*., 2010]. In such models, the increase of porosity during the acceleration of sliding induces a drop of the pore fluid pressure and thus an increase of the effective normal stress, thus inhibiting the instability. Using numerical modeling, *Yamashita* [1999] showed then that earthquake swarm-like rupture sequences can be simulated when the rate of pore creation is large enough during the sliding to inhibit the instability.

The analysis conducted here provides an explanation on how pore fluid pressures can be developed and maintained in fault zones and can thus be able to stress faults for weeks, months, or years (more than 2 years in the case of the 2003–2004 Ubaye swarm). Indeed, the low permeability of fault damage zones helps maintaining fluid overpressures developed by fault compaction in fault core zones. Fluid overpressures are thus trapped in the core zones and cannot escape easily because of the low permeability of surrounding rocks. In their study of faults characterized by high-permeability lenses of dolostone surrounded by low-permeability anhydrite layers, *Collettini et al*. [2009b] suggested that fluids entering in the high-permeability fault core lenses cannot escape easily due the low permeability of surrounding rocks. The conceptual model proposed in Figure 13 is thus consistent with the long-term duration of seismic swarms. However, further laboratory analyses to characterize the frictional properties of the fault gouge are required to characterize the stabilization mechanism during the 2003–2004 Ubaye seismic swarm that prevented the triggering of a large earthquake.

The hydromechanical modeling shows that pore fluid pressure buildup by elastic compaction is always lower than the value of the mechanical stressing, indicating an increase of the effective normal stress during fault compaction. The increase of the effective normal stress is incompatible with a weakening and reactivation of fault by elastic compaction. However, the transient release of pore fluid pressure by seismic-valve behavior during faulting might overpressure the surrounding rock masses and could potentially trigger earthquakes along adjacent fault planes prone to reactivation.

7. Conclusions

Based on an approach combining field observations, laboratory measurements, and hydromechanical modeling, this study shows the influence of the hydraulic and elastic heterogeneities of the constitutive elements of a mature fault on fault mechanics, and more specifically for fluid pressure buildup.

Laboratory measurements indicate that the physical properties of the studied fault differ from classical fault models. Indeed, the studied fault zone is characterized by a high-permeability, high-porosity, and low-rigidity core zone surrounded by a low-porosity, low-permeability, and high-rigidity damage zone. Microstructural analyses show that the hydraulic properties are controlled by S or C surface structures or foliations in fault core gouges and damage-zone phyllonites and by microcracks in the host gneisses, and that the elastic wave velocities are controlled by S or C surface structures or foliations in gneisses and phyllonites and by grain contacts in gouge. The development of these microstructures was achieved by the preferential brittle reactivation of weak mylonitic foliations during the Alpine history of the Argentera-Mercantour massif.

Our hydromechanical analysis shows that fluid overpressures can be developed and temporarily maintained in the studied fault zone by elastic compaction and that the development and maintenance of fluid overpressures are efficient in a high-porosity and low-rigidity fault core surrounded by a thick, low-porosity and low-permeability damage zone. The conceptual model proposed for fluid overpressure evolution through the fault zone is in agreement with the analyses conducted on seismic swarms and shows that the structure and physical properties of faults play a key role in earthquake swarm mechanics.

Acknowledgments

H. Leclère deeply thanks F. Passelègue, M. Rabin, H. Bourque, and D. Sanchez for their assistance during field work. The CNRS/INSU "Catastrophes Telluriques" program provided funding to F. Cappa and O. Fabbri. We thank J.P. Sizun for his help regarding porosity measurements, E. Mariani and C. Pinnington for SEM assistance, and G. Coughlan for technical assistance. Comments from C. Collettini and an anonymous reviewer helped clarifying the manuscript. The data shown in Figures 5, 6, and 8 can be obtained from the corresponding author.

References

Aoyama, H., M. Takeo, and S. Ide (2002), Evolution mechanisms of an earthquake swarm under the Hida Mountains, central Japan, in 1998, *J. Geophys. Res.*, *107*(B8), 2174, doi:10.1029/2001JB000540.

Armitage, P. J., D. R. Faulkner, R. H. Worden, A. C. Aplin, A. R. Butcher, and J. Iliffe (2011), Experimental measurement of, and controls on, permeability and permeability anisotropy of caprocks from the CO_2 storage project at the Krechba Field, Algeria, *J. Geophys. Res.*, *116*, B12208, doi:10.1029/2011JB008385.

Baietto, A., P. Perello, P. Cadoppi, and G. Martinotti (2009), Alpine tectonic evolution and thermal water circulations of the Argentera massif (South-Western Alps), *Swiss J. Geosci.*, *102*(2), 223–245, doi:10.1007/s00015-009-1313-5.

Behnsen, J., and D. R. Faulkner (2011), Water and argon permeability of phyllosilicate powders under medium to high pressure, *J. Geophys. Res.*, *116*, B12203, doi:10.1029/2011JB008600.
Behnsen, J., and D. R. Faulkner (2012), The effect of mineralogy and effective normal stress on frictional strength of sheet silicates, *J. Struct. Geol.*, *42*, 49–61, doi:10.1016/j.jsg.2012.06.015.
Belardinelli, M. E., M. Cocco, O. Coutant, and F. Cotton (1999), Redistribution of dynamic stress during coseismic ruptures: Evidence for fault interaction and earthquake triggering, *J. Geophys. Res.*, *104*(B7), 14,925–14,945, doi:10.1029/1999JB900094.
Benson, P., A. Schubnel, S. Vinciguerra, C. Trovato, P. Meredith, and R. P. Young (2006), Modeling the permeability evolution of microcracked rocks from elastic wave velocity inversion at elevated isostatic pressure, *J. Geophys. Res.*, *111*, B04202, doi:10.1029/2005JB003710.
Bigot-Cormier, F., M. Sosson, G. Poupeau, J.-F. Stéphan, and E. Labrin (2006), The denudation history of the Argentera Alpine external crystalline massif (Western Alps, France-Italy): An overview from the analysis of fission tracks in apatites and zircons, *Geodinamica Acta*, *19*(6), 455–473, doi:10.3166/ga.19.455-473.
Birch, F. (1960), The velocity of compressional waves in rocks to 10 kilobars: 1, *J. Geophys. Res.*, *65*(4), 1083–1102, doi:10.1029/JZ065i004p01083.
Blake, O. O., D. R. Faulkner, and A. Rietbrock (2013), The effect of varying damage history in crystalline rocks on the P- and S-wave velocity under hydrostatic confining pressure, *Pure Appl. Geophys.*, *170*(4), 493–505, doi:10.1007/s00024-012-0550-0.
Blanpied, M. L., D. A. Lockner, and J. D. Byerlee (1992), An earthquake mechanism based on rapid sealing of faults, *Nature*, *358*(6387), 574–576, doi:10.1038/358574a0.
Bogdanoff, S. (1986), Evolution de la partie occidentale du massif cristallin externe de l'Argentera. Place dans l'arc Alpin, *Geol. Fr.*, *4*, 433–453.
Bogdanoff, S., A. Michard, M. Mansour, and G. Poupeau (2000), Apatite fission track analysis in the Argentera massif: Evidence of contrasting denudation rates in the external crystalline massifs of the Western Alps, *Terra Nova*, *12*(3), 117–125, doi:10.1046/j.1365-3121.2000.123281.x.
Bourouis, S., and P. Bernard (2007), Evidence for coupled seismic and aseismic fault slip during water injection in the geothermal site of Soultz (France), and implications for seismogenic transients, *Geophys. J. Int.*, *169*(2), 723–732, doi:10.1111/j.1365-246X.2006.03325.x.
Boutareaud, S., C. A. J. Wibberley, O. Fabbri, and T. Shimamoto (2008), Permeability structure and co-seismic thermal pressurization on fault branches: Insights from the Usukidani fault, Japan, *Geol. Soc. London Spec. Publ.*, *299*(1), 341–361, doi:10.1144/SP299.20.
Brace, W. F., J. B. Walsh, and W. T. Frangos (1968), Permeability of granite under high pressure, *J. Geophys. Res.*, *73*(6), 2225–2236, doi:10.1029/JB073i006p02225.
Byerlee, J. (1993), Model for episodic flow of high-pressure water in fault zones before earthquakes, *Geology*, *21*(4), 303, doi:10.1130/0091-7613(1993)021<0303:MFEFOH>2.3.CO;2.
Caine, J. S., J. P. Evans, and C. B. Forster (1996), Fault zone architecture and permeability structure, *Geology*, *24*(11), 1025–1028, doi:10.1130/0091-7613(1996)024<1025:FZAAPS>2.3.CO;2.
Cappa, F. (2009), Modelling fluid transfer and slip in a fault zone when integrating heterogeneous hydromechanical characteristics in its internal structure, *Geophys. J. Int.*, *178*(3), 1357–1362, doi:10.1111/j.1365-246X.2009.04291.x.
Cappa, F. (2011), Influence of hydromechanical heterogeneities of fault zones on earthquake ruptures, *Geophys. J. Int.*, *185*(2), 1049–1058, doi:10.1111/j.1365-246X.2011.04994.x.
Cappa, F., J. Rutqvist, and K. Yamamoto (2009), Modeling crustal deformation and rupture processes related to upwelling of deep CO_2-rich fluids during the 1965–1967 Matsushiro earthquake swarm in Japan, *J. Geophys. Res.*, *114*, B10304, doi:10.1029/2009JB006398.
Chen, T.-M. N., W. Zhu, T. Wong, and S.-R. Song (2009), Laboratory characterization of permeability and its anisotropy of Chelungpu fault rocks, *Pure Appl. Geophys.*, *166*(5–7), 1011–1036, doi:10.1007/s00024-009-0497-y.
Chester, F. M., and J. M. Logan (1986), Implications for mechanical properties of brittle faults from observations of the Punchbowl fault zone, California, *Pure Appl. Geophys.*, *124*(1–2), 79–106, doi:10.1007/BF00875720.
Chouliaras, G., G. Drakatos, K. Pavlou, and K. Makropoulos (2013), Stress distribution and seismicity patterns of the 2011 seismic swarm in the Messinia basin, (south-western Peloponnesus), Greece, *Nat. Hazards Earth Syst. Sci.*, *13*(1), 45–51, doi:10.5194/nhess-13-45-2013.
Collettini, C., and R. H. Sibson (2001), Normal faults, normal friction?, *Geology*, *29*(10), 927–930, doi:10.1130/0091-7613(2001)029<0927:NFNF>2.0.CO;2.
Collettini, C., A. Niemeijer, C. Viti, and C. Marone (2009a), Fault zone fabric and fault weakness, *Nature*, *462*(7275), 907–910, doi:10.1038/nature08585.
Collettini, C., N. De Paola, and D. R. Faulkner (2009b), Insights on the geometry and mechanics of the Umbria–Marche earthquakes (Central Italy) from the integration of field and laboratory data, *Tectonophysics*, *476*(1–2), 99–109, doi:10.1016/j.tecto.2008.08.013.
Cornet, F. H., J. Helm, H. Poitrenaud, and A. Etchecopar (1997), Seismic and aseismic slips induced by large-scale fluid injections, *Pure Appl. Geophys.*, *150*, 563–583.
Corsini, M., G. Ruffet, and R. Caby (2004), Alpine and Late-Hercynian geochronological constraints in the Argentera massif (Western Alps), *Eclogae Geol. Helv.*, *97*(1), 3–15, doi:10.1007/s00015-004-1107-8.
Crawford, B. R., D. R. Faulkner, and E. H. Rutter (2008), Strength, porosity, and permeability development during hydrostatic and shear loading of synthetic quartz-clay fault gouge, *J. Geophys. Res.*, *113*, B03207, doi:10.1029/2006JB004634.
Daniel, G., et al. (2011), Changes in effective stress during the 2003–2004 Ubaye seismic swarm, France, *J. Geophys. Res.*, *116*, B01309, doi:10.1029/2010JB007551.
Detournay, E., and A. H.-D. Cheng (1993), Fundamentals of poroelasticity, in *Comprehensive Rock Engineering: Principles, Practice and Projects*, *Analysis and Design Method*, vol. II, edited by C. Fairhurst, pp. 113–171, Pergamon Press, New York.
Evans, J. P., C. B. Forster, and J. V. Goddard (1997), Permeability of fault-related rocks, and implications for hydraulic structure of fault zones, *J. Struct. Geol.*, *19*(11), 1393–1404, doi:10.1016/S0191-8141(97)00057-6.
Faulkner, D. R. (2004), A model for the variation in permeability of clay-bearing fault gouge with depth in the brittle crust, *Geophys. Res. Lett.*, *31*, L19611, doi:10.1029/2004GL020736.
Faulkner, D. R., and P. J. Armitage (2013), The effect of tectonic environment on permeability development around faults and in the brittle crust, *Earth Planet. Sci. Lett.*, *375*, 71–77, doi:10.1016/j.epsl.2013.05.006.
Faulkner, D. R., and E. H. Rutter (1998), The gas permeability of clay-bearing fault gouge at 20 °C, *Geol. Soc. London Spec. Publ.*, *147*(1), 147–156, doi:10.1144/GSL.SP.1998.147.01.10.
Faulkner, D. R., and E. H. Rutter (2001), Can the maintenance of overpressured fluids in large strike-slip fault zones explain their apparent weakness?, *Geology*, *29*(6), 503–506, doi:10.1130/0091-7613(2001)029<0503:CTMOOF>2.0.CO;2.
Faulkner, D. R., A. C. Lewis, and E. H. Rutter (2003), On the internal structure and mechanics of large strike-slip fault zones: Field observations of the Carboneras fault in southeastern Spain, *Tectonophysics*, *367*(3–4), 235–251, doi:10.1016/S0040-1951(03)00134-3.
Faulkner, D. R., T. M. Mitchell, D. Healy, and M. J. Heap (2006), Slip on "weak" faults by the rotation of regional stress in the fracture damage zone, *Nature*, *444*(7121), 922–925, doi:10.1038/nature05353.

Faulkner, D. R., T. M. Mitchell, E. Jensen, and J. Cembrano (2011), Scaling of fault damage zones with displacement and the implications for fault growth processes, *J. Geophys. Res.*, *116*, B05403, doi:10.1029/2010JB007788.

Faure-Muret, A. (1955), Etudes géologiques sur le massif de l'Argentera-Mercantour et ses enveloppes sédimentaires, *Mémoire de la Société Géologique de France*, p. 336.

Ferrara, G., and M. Malaroda (1969), Radiometric age of granitic rocks from the Argentera massif (Maritime Alps), *Boll. Soc. Geol. Italienna*, *88*, 311–320.

Ford, A., T. Blenkinsop, and J. McLellan (2009), Factors affecting fluid flow in strike-slip fault systems: Coupled deformation and fluid flow modelling with application to the western Mount Isa Inlier, Australia, *Geofluids*, *9*(1), 2–23, doi:10.1111/j.1468-8123.2008.00219.x.

Gratier, J.-P., P. Favreau, and F. Renard (2003), Modeling fluid transfer along California faults when integrating pressure solution crack sealing and compaction processes, *J. Geophys. Res.*, *108*(B2), 2104, doi:10.1029/2001JB000380.

Hainzl, S., T. Kraft, J. Wassermann, H. Igel, and E. Schmedes (2006), Evidence for rainfall-triggered earthquake activity, *Geophys. Res. Lett.*, *33*, L19303, doi:10.1029/2006GL027642.

Heikamp, S., and G. Nover (2003), An integrated study on physical properties of a KTB gneiss sample and marble from Portugal: Pressure dependence of the permeability and frequency dependence of the complex electrical impedance, in *Thermo-Hydro-Mechanical Coupling in Fractured Rock*, edited by H.-J. Kümpel, pp. 929–936, Birkhäuser, Basel.

Ikari, M. J., D. M. Saffer, and C. Marone (2009), Frictional and hydrologic properties of clay-rich fault gouge, *J. Geophys. Res.*, *114*, B05409, doi:10.1029/2008JB006089.

Itasca Consulting Group (2006), FLAC3D, Fast Lagrangian Analysis of Continua in 3 dimensions, Version 3.0. Five volumes, *Itasca Consulting Group*, Minneapolis, Minn.

Jefferies, S. P., R. E. Holdsworth, C. A. J. Wibberley, T. Shimamoto, C. J. Spiers, A. R. Niemeijer, and G. E. Lloyd (2006), The nature and importance of phyllonite development in crustal-scale fault cores: An example from the Median Tectonic Line, Japan, *J. Struct. Geol.*, *28*(2), 220–235, doi:10.1016/j.jsg.2005.10.008.

Jenatton, L., R. Guiguet, F. Thouvenot, and N. Daix (2007), The 16,000-event 2003–2004 earthquake swarm in Ubaye (French Alps), *J. Geophys. Res.*, *112*, B11304, doi:10.1029/2006JB004878.

Jeppson, T. N., K. K. Bradbury, and J. P. Evans (2010), Geophysical properties within the San Andreas fault zone at the San Andreas fault observatory at depth and their relationships to rock properties and fault zone structure, *J. Geophys. Res.*, *115*, B12423, doi:10.1029/2010JB007563.

Kerckhove, C. (1969), La zone du flysch dans les nappes de l'Embrunais-Ubaye (Alpes Occidentales), *Geol. Alp.*, *45*, 1–202.

Kerckhove, C., J. C. Barfety, S. Bogdanoff, F. Carraro, M. Gidon, M. Jorda, M. Lemoine, R. Malaroda, and G. Montjuvent (1980), Feuille de Gap, Carte Géol. France, Map 35, scale 1:250000, *Bureau de Recherches Géologiques et Minières*, Orléans, France.

Kilb, D., J. Gomberg, and P. Bodin (2000), Triggering of earthquake aftershocks by dynamic stresses, *Nature*, *408*(6812), 570–574, doi:10.1038/35046046.

King, G. C. P., R. S. Stein, and J. Lin (1994), Static stress changes and the triggering of earthquakes, *Bull. Seismol. Soc. Am.*, *84*(3), 935–953.

Kuttruff, H. (1991), *Ultrasonics Fundamentals and Applications*, Elsevier Science & Technology, New York.

Leclère, H., O. Fabbri, G. Daniel, and F. Cappa (2012a), Reactivation of a strike-slip fault by fluid overpressuring in the southwestern French–Italian Alps, *Geophys. J. Int.*, *189*(1), 29–37, doi:10.1111/j.1365-246X.2011.05345.x.

Leclère, H., M. Buatier, D. Charpentier, J.-P. Sizun, P. Labaume, and T. Cavailhes (2012b), Formation of phyllosilicates in a fault zone affecting deeply buried arkosic sandstones: Their influence on petrophysic properties (Annot sandstones, French external Alps), *Swiss J. Geosci.*, *105*(2), 299–312, doi:10.1007/s00015-012-0099-z.

Leclère, H., G. Daniel, O. Fabbri, F. Cappa, and F. Thouvenot (2013), Tracking fluid pressure buildup from focal mechanisms during the 2003–2004 Ubaye seismic swarm, France, *J. Geophys. Res. Solid Earth*, *118*, 4461–4476, doi:10.1002/jgrb.50297.

Lockner, D. A., and J. D. Byerlee (1994), Dilatancy in hydraulically isolated faults and the suppression of instability, *Geophys. Res. Lett.*, *21*(22), 2353–2356, doi:10.1029/94GL02366.

Lockner, D. A., H. Tanaka, H. Ito, R. Ikeda, K. Omura, and H. Naka (2009), Geometry of the Nojima fault at Nojima-Hirabayashi, Japan—I. A simple damage structure inferred from borehole core permeability, *Pure Appl. Geophys.*, *166*(10–11), 1649–1667, doi:10.1007/s00024-009-0515-0.

Lohman, R. B., and J. J. McGuire (2007), Earthquake swarms driven by aseismic creep in the Salton Trough, California, *J. Geophys. Res.*, *112*, B04405, doi:10.1029/2006JB004596.

Malaroda, R., F. Carraro, G. V. Dal Piaz, B. Franceschetti, C. Sturani, and E. Zanella (1970), Carta geologica del Massicio dell'Argentera alla scala 1:50000 e Note illustrative, *Memoria della Societa Geologica*, A. IX, 557–663.

Mariani, E., K. H. Brodie, and E. H. Rutter (2006), Experimental deformation of muscovite shear zones at high temperatures under hydrothermal conditions and the strength of phyllosilicate-bearing faults in nature, *J. Struct. Geol.*, *28*(9), 1569–1587, doi:10.1016/j.jsg.2006.06.009.

Marone, C., C. B. Raleigh, and C. H. Scholz (1990), Frictional behavior and constitutive modeling of simulated fault gouge, *J. Geophys. Res.*, *95*(B5), 7007–7025, doi:10.1029/JB095iB05p07007.

Miller, S. A., C. Collettini, L. Chiaraluce, M. Cocco, M. Barchi, and B. J. P. Kaus (2004), Aftershocks driven by a high-pressure CO_2 source at depth, *Nature*, *427*(6976), 724–727, doi:10.1038/nature02251.

Mitchell, T. M., and D. R. Faulkner (2008), Experimental measurements of permeability evolution during triaxial compression of initially intact crystalline rocks and implications for fluid flow in fault zones, *J. Geophys. Res.*, *113*, B11412, doi:10.1029/2008JB005588.

Mittempergher, S., G. Pennacchioni, and G. Di Toro (2009), The effects of fault orientation and fluid infiltration on fault rock assemblages at seismogenic depths, *J. Struct. Geol.*, *31*(12), 1511–1524, doi:10.1016/j.jsg.2009.09.003.

Mizoguchi, K., T. Hirose, T. Shimamoto, and E. Fukuyama (2008), Internal structure and permeability of the Nojima fault, southwest Japan, *J. Struct. Geol.*, *30*(4), 513–524, doi:10.1016/j.jsg.2007.12.002.

Monié, P., and H. Maluski (1983), Données chronologiques $^{40}Ar/^{39}Ar$ sur le socle anté- Permien de l'Argentera- Mercantour (Alpes Maritimes, France), *Bull. Soc. Geol. Fr.*, *7*(2), 247–257.

Moore, D. E., and D. A. Lockner (2004), Crystallographic controls on the frictional behavior of dry and water-saturated sheet structure minerals, *J. Geophys. Res.*, *109*, B03401, doi:10.1029/2003JB002582.

Morrow, C. A., L. Q. Shi, and J. D. Byerlee (1984), Permeability of fault gouge under confining pressure and shear stress, *J. Geophys. Res.*, *89*(B5), 3193–3200, doi:10.1029/JB089iB05p03193.

Morrow, C., D. Lockner, S. Hickman, M. Rusanov, and T. Röckel (1994), Effects of lithology and depth on the permeability of core samples from the Kola and KTB drill holes, *J. Geophys. Res.*, *99*(B4), 7263–7274, doi:10.1029/93JB03458.

Musumeci, G., and F. Colombo (2002), Late Visean mylonitic granitoids in the Argentera Massif (western Alps, Italy): Age and kinematic constraints on the Ferrière–Mollières shear zone, *C. R. Geosci.*, *334*(3), 213–220, doi:10.1016/S1631-0713(02)01722-4.

Numelin, T., C. Marone, and E. Kirby (2007), Frictional properties of natural fault gouge from a low-angle normal fault, Panamint Valley, California, *Tectonics*, *26*, TC2004, doi:10.1029/2005TC001916.
Nur, A. (1974), Matsushiro, Japan, earthquake swarm: Confirmation of the dilatancy-fluid diffusion model, *Geology*, *2*(5), 217, doi:10.1130/0091-7613(1974)2<217:MJESCO>2.0.CO;2.
Nur, A., and J. R. Booker (1972), Aftershocks caused by pore fluid flow?, *Science*, *175*(4024), 885–887, doi:10.1126/science.175.4024.885.
Paquette, J.-L., R.-P. Menot, and J.-J. Peucat (1989), REE, SmNd and UPb zircon study of eclogites from the Alpine external massifs (Western Alps): Evidence for crustal contamination, *Earth Planet. Sci. Lett.*, *96*(1–2), 181–198, doi:10.1016/0012-821X(89)90131-3.
Rice, J. R. (1992), Fault stress states, pore pressure distributions, and the weakness of the San Andreas fault, in *Fault Mechanics and Transport Properties of Rocks*, edited by B. Evans and T. F. Wong, pp. 475–503, Academic Press, London.
Rigot, A., N. Béthoux, F. Masson, and J.-F. Ritz (2008), Seismicity rate and wave-velocity variations as consequences of rainfall: The case of the catastrophic storm of September 2002 in the Nîmes fault region (Gard, France), *Geophys. J. Int.*, *173*(2), 473–482, doi:10.1111/j.1365-246X.2008.03718.x.
Rubatto, D., U. Schaltegger, B. Lombardo, F. Colombo, and R. Compagnoni (2001), Complex Paleozoic magmatic and metamorphic evolution in the Argentera massif (Western Alps) resolved with U–Pb dating, *Schweiz. Mineral. Petrogr. Mitt.: Mineral. Petrogr.*, *81*, 213–228.
Sanchez, G., Y. Rolland, J. Schneider, M. Corsini, E. Oliot, P. Goncalves, C. Verati, J.-M. Lardeaux, and D. Marquer (2011a), Dating low-temperature deformation by 40Ar/39Ar on white mica, insights from the Argentera-Mercantour massif (SW Alps), *Lithos*, *125*(1–2), 521–536, doi:10.1016/j.lithos.2011.03.009.
Sanchez, G., Y. Rolland, M. Jolivet, S. Brichau, M. Corsini, and A. Carter (2011b), Exhumation controlled by transcurrent tectonics: The Argentera–Mercantour massif (SW Alps), *Terra Nova*, *23*(2), 116–126, doi:10.1111/j.1365-3121.2011.00991.x.
Schmid, S. M., B. Fügenschuh, E. Kissling, and R. Schuster (2004), Tectonic map and overall architecture of the Alpine orogen, *Eclogae Geol. Helv.*, *97*(1), 93–117, doi:10.1007/s00015-004-1113-x.
Segall, P., and J. R. Rice (1995), Dilatancy, compaction, and slip instability of a fluid-infiltrated fault, *J. Geophys. Res.*, *100*, 22,155–22,171, doi:10.1029/95JB02403.
Segall, P., A. M. Rubin, A. M. Bradley, and J. R. Rice (2010), Dilatant strengthening as a mechanism for slow slip events, *J. Geophys. Res.*, *115*, B12305, doi:10.1029/2010JB007449.
Sheldon, H. A., and A. Ord (2005), Evolution of porosity, permeability and fluid pressure in dilatant faults post-failure: Implications for fluid flow and mineralization, *Geofluids*, *5*(4), 272–288, doi:10.1111/j.1468-8123.2005.00120.x.
Shipton, Z. K., A. M. Soden, J. D. Kirkpatrick, A. M. Bright, and R. J. Lunn (2006), How thick is a fault? Fault displacement-thickness scaling revisited, in *Radiated Energy and the Physics of Faulting*, *Geophys. Monogr. Ser.*, vol. 170, edited by R. Abercrombie et al., pp. 193–198, AGU, Washington, D. C.
Sibson, R. H. (1977), Fault rocks and fault mechanisms, *J. Geol. Soc.*, *133*(3), 191–213, doi:10.1144/gsjgs.133.3.0191.
Sibson, R. H. (1990), Rupture nucleation on unfavorably oriented faults, *Bull. Seismol. Soc. Am.*, *80*(6A), 1580–1604.
Sibson, R. H. (2009), Rupturing in overpressured crust during compressional inversion: The case from NE Honshu, Japan, *Tectonophysics*, *473*(3–4), 404–416, doi:10.1016/j.tecto.2009.03.016.
Sleep, N. H., and M. L. Blanpied (1992), Creep, compaction and the weak rheology of major; faults, *Nature*, *359*(6397), 687–692, doi:10.1038/359687a0.
Stein, R. S. (1999), The role of stress transfer in earthquake occurrence, *Nature*, *402*(6762), 605–609, doi:10.1038/45144.
Tanikawa, W., and T. Shimamoto (2009), Frictional and transport properties of the Chelungpu fault from shallow borehole data and their correlation with seismic behavior during the 1999 Chi-Chi earthquake, *J. Geophys. Res.*, *114*, B01402, doi:10.1029/2008JB005750.
Terakawa, T., A. Zoporowski, B. Galvan, and S. A. Miller (2010), High-pressure fluid at hypocentral depths in the L'Aquila region inferred from earthquake focal mechanisms, *Geology*, *38*(11), 995–998, doi:10.1130/G31457.1.
Tsutsumi, A., S. Nishino, K. Mizoguchi, T. Hirose, S. Uehara, K. Sato, W. Tanikawa, and T. Shimamoto (2004), Principal fault zone width and permeability of the active Neodani fault, Nobi fault system, Southwest Japan, *Tectonophysics*, *379*(1–4), 93–108, doi:10.1016/j.tecto.2003.10.007.
Uehara, S., and T. Shimamoto (2004), Gas permeability evolution of cataclasite and fault gouge in triaxial compression and implications for changes in fault-zone permeability structure through the earthquake cycle, *Tectonophysics*, *378*(3–4), 183–195, doi:10.1016/j.tecto.2003.09.007.
Walker, R. J., R. E. Holdsworth, P. J. Armitage, and D. R. Faulkner (2013), Fault zone permeability structure evolution in basalts, *Geology*, *41*(1), 59–62, doi:10.1130/G33508.1.
Wang, Q., and S. Ji (2009), Poisson's ratios of crystalline rocks as a function of hydrostatic confining pressure, *J. Geophys. Res.*, *114*, B09202, doi:10.1029/2008JB006167.
Wibberley, C. A. J. (2002), Hydraulic diffusivity of fault gouge zones and implications for thermal pressurization during seismic slip, *Earth Planets Space*, *54*(11), 1153–1171, doi:10.1186/BF03353317.
Wibberley, C. A. J., and T. Shimamoto (2003), Internal structure and permeability of major strike-slip fault zones: The Median Tectonic Line in Mie Prefecture, Southwest Japan, *J. Struct. Geol.*, *25*(1), 59–78, doi:10.1016/S0191-8141(02)00014-7.
Wicks, C., W. Thelen, C. Weaver, J. Gomberg, A. Rohay, and P. Bodin (2011), InSAR observations of aseismic slip associated with an earthquake swarm in the Columbia River flood basalts, *J. Geophys. Res.*, *116*, B12304, doi:10.1029/2011JB008433.
Yamashita, T. (1999), Pore creation due to fault slip in a fluid-permeated fault zone and its effect on seismicity: Generation mechanism of earthquake swarm, in *Seismicity Patterns, Their Statistical Significance and Physical Meaning*, edited by M. Wyss, K. Shimazaki, and A. Ito, pp. 625–647, Birkhäuser, Basel.
Yang, Y., and A. C. Aplin (2007), Permeability and petrophysical properties of 30 natural mudstones, *J. Geophys. Res.*, *112*, B03206, doi:10.1029/2005JB004243.
Yukutake, Y., H. Ito, R. Honda, M. Harada, T. Tanada, and A. Yoshida (2011), Fluid-induced swarm earthquake sequence revealed by precisely determined hypocenters and focal mechanisms in the 2009 activity at Hakone volcano, Japan, *J. Geophys. Res.*, *116*, B04308, doi:10.1029/2010JB008036.
Zhang, S., T. E. Tullis, and V. J. Scruggs (1999), Permeability anisotropy and pressure dependency of permeability in experimentally sheared gouge materials, *J. Struct. Geol.*, *21*(7), 795–806, doi:10.1016/S0191-8141(99)00080-2.
Zhang, S., T. E. Tullis, and V. J. Scruggs (2001), Implications of permeability and its anisotropy in a mica gouge for pore pressures in fault zones, *Tectonophysics*, *335*(1–2), 37–50, doi:10.1016/S0040-1951(01)00044-0.
Zhang, Y., P. M. Schaubs, C. Zhao, A. Ord, B. E. Hobbs, and A. C. Barnicoat (2008), Fault-related dilation, permeability enhancement, fluid flow and mineral precipitation patterns: Numerical models, *Geol. Soc. London Spec. Publ.*, *299*(1), 239–255, doi:10.1144/SP299.15.